

MICROSTRUCTURE-SENSITIVE PLASTICITY AND
FATIGUE MODELING OF EXTRUDED
6061 ALUMINUM ALLOYS

by

ROBERT ROSS MCCULLOUGH

J. BRIAN JORDON, COMMITTEE CHAIR
MARK BARKEY
BETH TODD

A THESIS

Submitted in partial fulfillment of the requirements
for the degree of Master of Science in the
Department of Mechanical Engineering
in the Graduate School of
The University of Alabama

TUSCALOOSA, ALABAMA

2014

Copyright Robert Ross McCullough 2014
ALL RIGHTS RESERVED

ABSTRACT

In this study, the development of fatigue failure and stress anisotropy in light weight ductile metal alloys, specifically Al-Mg-Si aluminum alloys, was investigated. The experiments were carried out on an extruded 6061 aluminum alloy. Reverse loading experiments were performed up to a prestrain of 5% in both tension-followed-by-compression and compression-followed-by-tension. The development of isotropic and kinematic hardening and subsequent anisotropy was indicated by the observation of the Bauschinger effect phenomenon.

Experimental results show that 6061 aluminum alloy exhibited a slight increase in the kinematic hardening versus applied prestrain. However, the ratio of kinematic-to-isotropic hardening remained near unity. An internal state variable (ISV) plasticity and damage model was used to capture the evolution of the anisotropy for the as-received T6 and partially annealed conditions.

Following the stress anisotropy experiments, the same extruded 6061 aluminum alloy was tested under fully reversing, strain-controlled low cycle fatigue at up to 2.5% strain amplitudes and two heat treatment conditions. Observations were made of the development of striation fields up to the point of nucleation at cracked and clustered precipitants and free surfaces through localized precipitant slip band development. A finite element enabled micromechanics study of fatigue damage development of local strain field in the presence of hard phases was conducted. Both the FEA and experimental data sets were utilized in the implementation of a multi-stage fatigue model in order to predict the microstructure response, including fatigue nucleation and propagation contributions on the total fatigue life in AA6061.

Good correlation between experimental and predicted results in the number of cycles to final failure was observed. The AA6061 material maintained relatively consistent low cycle fatigue performance despite two different heat treatments.

DEDICATION

This thesis is dedicated first all to God for giving me the vision and strength to carry out this work and second to my family and friends for their never failing moral and intellectual support throughout this study.

ACKNOWLEDGEMENTS

This work has been enabled by a special group of which I would like to acknowledge. First, I want to thank Dr. Jordon for his long-term guidance and support as my advisor and friend in developing and executing this project. Second, my thanks to Dr. Todd for her faithful support throughout my academic career and for allowing me to participate in the GK12 STEM program. Also, I want to express my deep appreciation to Dr. Mark Barkey for being a mentor to me as I have developed my career as an engineer and researcher, providing me with expertise and guidance throughout my work. I would also like to acknowledge my colleagues, Rogie Rodriguez, Joao Moraes, and Dr. Harish Rao for providing me with accountability and encouragement while conducting this research project and the subsequent studies. I also want to acknowledge Dr. Paul Allison from the Army Corps. Of Engineers Engineer Research & Development Center for his financial and technical support that made this research possible. A portion of this work was performed under the auspices of the U.S. Army Research Office Scientific Services Program administered by Battelle Memorial Institute, Contract No. W911NF-11-D-0001. Permission to publish was granted by Director, Geotechnical and Structures Laboratory.

CONTENTS

ABSTRACT	ii
DEDICATION	i
ACKNOWLEDGEMENTS	ii
LIST OF TABLES	v
LIST OF FIGURES	ix
INTRODUCTION	1
BACKGROUND	3
Bauschinger Effect.....	3
Fatigue in Light Weight Alloys	7
EXPERIMENTS AND MATERIALS	9
Material Preparation.....	9
Mechanical Characterization	10
Microstructure Characterization	10
COMPUTATIONAL MODEL.....	12
ISV Plasticity Damage Model	12
Multi-Stage Fatigue Model.....	17
Stages of Fatigue Damage.....	17

Crack Incubation.....	18
Small Crack	20
Long Crack	21
RESULTS AND DISCUSSION.....	23
Microstructure.....	23
Monotonic and Cyclic Stress/Strain Response	26
Mechanical Evaluation of the Bauschinger Effect.....	27
Experimental Fatigue Response.....	32
Fractography	35
Micromechanics Simulations.....	39
Fatigue Model Correlation	41
CONCLUSIONS.....	46
REFERENCES	49

LIST OF TABLES

Table 1. Relationship functions for ISV plasticity model.....	16
Table 2. Monotonic tensile properties of 6061 aluminum alloy.....	26
Table 3. Bauschinger effect results by prestrain for AA6061 aluminum alloy	28
Table 4. ISV model plasticity and damage constants	29
Table 5. Monotonic tensile/microstructure properties	32
Table 6. Cyclic/fatigue parameters	34
Table 7. Microstructure-property MSF model coefficients	41

LIST OF FIGURES

Figure 1. Illustration of the Bauschinger effect typically seen in ductile materials. Adapted from (Chun, Jinn, and Lee 2002; Eggertsen and Mattiasson 2009)	4
Figure 2. Optical images of etched AA6061 in (A) as-received and (B) annealed states.	23
Figure 3. Electron backscatter diffraction results for 6061 aluminum alloy with IPF charts oriented in the extruded direction (A and B), pole figure (C and D), and the misorientation angle chart (E).....	24
Figure 4. Micrograph (A) of observed Ferrite-rich, Silicon-based intermetallic particles and the corresponding chemical analysis (B).....	25
Figure 5. Monotonic and Cyclic Stress/Strain Plot.....	27
Figure 6. BSP and RKI ratio plotted versus applied forward prestrain in (A) tension-followed-by-compression and (B) compression-followed-by-tension.	29
Figure 7. Fractured particles after 5% pre-strain in compression-followed-by-tension.	31
Figure 8. ISV model correlation to experimental results at (A) 3% pre-strain and (B) 5% pre-strain in tension-followed-by compression and compression-followed-by tension.	32
Figure 9. Strain amplitude plot of fully reversing fatigue data from as-received and annealed states.....	33
Figure 10. First cycle (a) and half-life (b) hysteresis loop plots for as-received and annealed states.....	34
Figure 11. Fatigue life plot for as-received and annealed states.....	35
Figure 12. SEM fractography (R=-1) of as-received aa6061 a) 0.7% & b) 1.0% strain amplitude.	37
Figure 13. SEM fractography (R=-1) of annealed aa6061 a) 1.0% & b) 2.5% strain amplitude.	38
Figure 14. (a) FEA microstructure simulation illustration, (b) generated plasticity field contour map, (c) local plastic strain to remote strain plot & (d) l/d to remote strain plot.	40
Figure 15. MSF crack growth model sensitivity charts a) as-received & b) annealed.	42

Figure 16. Fully reversing fatigue plot with MSF incubation and total strain-life results..... 43

Figure 17. MSF fatigue fit plots for (a) as-received & (b) annealed states with upper and lower boundaries formed by $\pm \frac{1}{2}$ std. dev of the mean particle size. 44

Figure 18. Predicted percentage contribution of incubation life to total fatigue life of as-received and annealed states..... 45

INTRODUCTION

Precipitant hardened aluminum alloys make up one of the most widely utilized material groups within the industry, both due to their ease of manufacture and excellent manufacturing properties(W. . Miller et al. 2000). Out of these alloys, heat treatable Aluminum-Magnesium-Silicon alloys have long been a major material system for many applications due to their versatile collection of properties that make them ideal as structural materials(Q Wang, Kawagoishi, and Chen 2006; Ozturk et al. 2010). These properties include intermediate mechanical strength, strong corrosion resistance, excellent strength-to-weight ratios and good formability, which can be attributed to the presence of nano- to micro-length scale precipitants, containing these magnesium and silicon alloying elements, in addition to the trace elements normally seen within the matrix(Zhao 2013).

In application, the ability to understand and model the development and propagation of plasticity damage in alloys is an important cornerstone of modern engineering and a key focus of material research for the past two decades. The current demand for weight reduction and energy efficiency has given rise to the increased implementation of advanced material systems, like

AA6061 . The growing prevalence of these materials in a wide range of industries from automotive to architectural systems has greatly increased the need to be able to accurately and effectually predict the overall response of the material to loading. This need is prominent in the capture of the onset and progression of strain hardening and failure with in these material systems.

In this work, a plasticity study of AA6061 in a T6 heat treatment condition has has been conducted. This study is focused on both experimental characterization and modeling of plasticity damage mechanics using an internal variable model approach. Using key microstructure features, the evolution of damage was correlated to the development of the flow stress anisotropy phenomena commonly referred to as the Bauschinger effect. This work also presents fully reversing, stain-controlled fatigue experiments and scanning electron microscopy fractographic analysis for the same 6061-T6 aluminum alloy. The derived structural properties were implemented into a microstructural finite element model in order to capture the fatigue crack incubation behavior due to the influence of discontinuously distributed hard precipitates. Data generated from this analysis was implemented into a microstructural-based fatigue model. A summary will be made of the results of the studies performed in this project.

BACKGROUND

Bauschinger Effect

The concept of the Bauschinger effect has long been understood as being a phenomenon of the development and evolution of long range internal stress or backstress within a solid material matrix. With recent trends moving towards creating lightweight and high efficiency designs, incorporating the BE in material models is vital for accurately predicting the cyclic stress-strain response of ductile, metallic materials. From a homogeneous material perspective, the Bauschinger effect is the occurrence of reduced flow stress during reversing of initially applied loading, see Figure 1. In Figure 1, segment (A-B) represents the actual reversing loading curve in compression after tension. (A-B') is an inverted, representative curve of (A-B) to enhance comparison between forward and reverse loading segments. Segment (A-B'') shows the differences between the expected monotonic flow stresses and observed cyclic response under BE.

Development of the stress flow anisotropy and therefore BE in polycrystalline metals is closely tied the evolution of internal stress due to both static and dynamic strain histories (Kishi and Tanabe 1973). The BE has been noted as being significantly impacted by the material's response to cyclic deformation through the reduction of such characteristics as; strain hardening rate, failure stresses, and elastic limit (reverse yielding) (Tamura et al. 2011; Liao, Kao, and Chang 1997; Liangsen and Xinghua 1999; Bate and Wilson 1986; Yoshimura and Kenkyūjo 1959; Yoshimura, Daigaku, and Kenkyjo 1959; Lloyd 1977; Kassner et al. 2008).

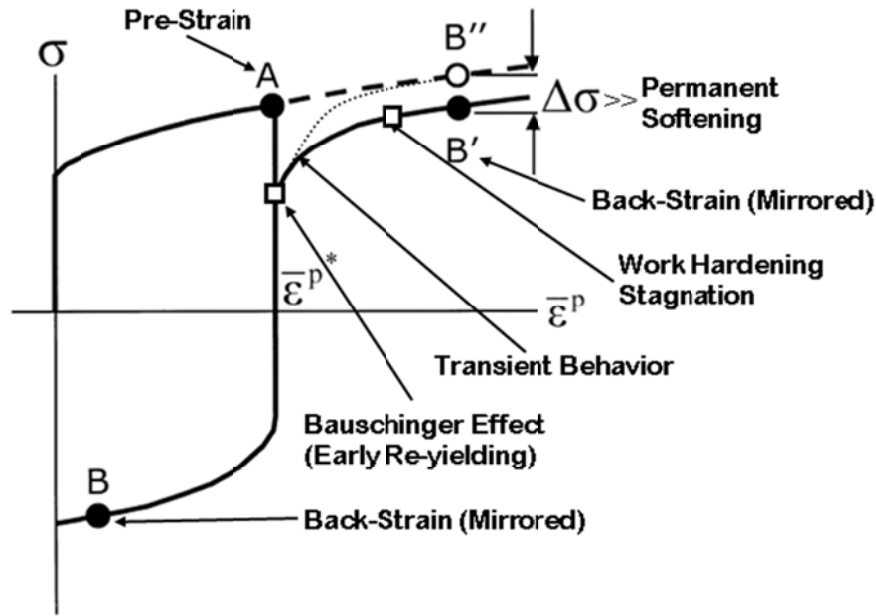


Figure 1. Illustration of the Bauschinger effect typically seen in ductile materials. Adapted from (Chun, Jinn, and Lee 2002; Eggertsen and Mattiasson 2009)

In polycrystalline metals, as prevalently seen in both steels and aluminum alloys, grain alignment and differences in flow-stress between intergranular regions, grain boundaries and second phase particles act as active determinates of both the onset of the BE and its magnitude (Margolin, Hazaveh, and Yaguchi 1978; Richeton, Berbenni, and Berveiller 2009; Buckley and Entwistle 1956). Finite element analysis (FEA) modeling has shown that deformation-induced anisotropic behavior can be captured by considering a heterogeneous pattern of the load distribution through the microstructure. In fact, FEA can capture load transients over a large range of strains even in the presence of limited dislocation driven strain hardening (Gan et al. 2006). Transmission electron microscopy (TEM) observations further confirm this, as the onset of BE in nano-grain metals was shown to be unrelated to grain size, but rather heterogeneity of the microstructure and subsequently load distribution (Rajagopalan et al. 2010). Dispersion hardened metallic alloys have also been shown to have significant sensitivity to variation in backstress and its effect on kinematic hardening (Gould, Hirsch, and Humphreys 1974;

Hidayetoglu, Pica, and Haworth 1985; Lloyd 1977; Ozturk et al. 2010; Reynolds and Lyons 1997), with BE amplified with increased volume fraction of particles and composites, such as Silicon Carbide (SiC) whisker and particle reinforced aluminum (Arsenault and Wu 1987; Taya et al. 1990; Corbin, Wilkinson, and Embury 1996). In addition, the aging state of the material is also observed to produce a change in anisotropy behavior due to the evolution of dislocation mechanisms, specifically Orowan Loops, around precipitates which are more readily sheared in overaged states (Myriounis, Hasan, and Matikas 2008; Bonollo, Ceschini, and Garagnani 1997).

In recent years, research has shown that accounting for only back stresses, a foundational component in early plasticity models, within a material is not sufficient to fully explain the development of BE (Kassner et al. 2008; Xiang and Vlassak 2005; Yoshida and Uemori 2002). Mechanisms such as the Orowan-Sleeswyk effect in conjunction with long-range internal stresses generally captured the development of the BE within polycrystalline material (Kassner et al. 2008). As such, it has become well established that dislocation theory is effective in capturing the evolution of plasticity in polycrystalline metals. This observation was shown to be very effective when focused on the transient effects of short range mechanisms, such as resistance to motion or long range, including pinning and pile up at grain boundaries or precipitants (Orowan Loops). Thus, dislocation theory is well established as a major component in the evolution of mechanical response in metals due to their deformation history (Woolley 1953; Abel and Muir 1972; Abel 1987; O. B. Pedersen, Brown, and Stobbs 1981; Proudhon et al. 2008; Lassance et al. 2007).

At the macroscale, the observations of the BE in crystalline structured materials typically centered on the decrease in reverse yield stress. From an engineering perspective, this effect can be directly quantified at the macroscale by the ratio between the development of the forward and

reverse stress. This formulation, see equation 1, is referred to as the Bauschinger Stress Parameter (BSP) (Caceres, Griffiths, and Reiner 1996) and has been applied to various aluminum alloys (Mark F Horstemeyer 1998; Embury 1987).

$$BSP = \frac{|\sigma_f| - |\sigma_r|}{|\sigma_f|} \quad (1)$$

While the BSP can generally quantify the BE, it does not explicitly quantify the degree of kinematic and isotropic hardening present during reverse yield loading. By using the concept of yield surface for both the kinematic and isotropic strain hardening relationships, a ratio (RKI), equation 2, can be used to quantify the BE:

$$RKI = \frac{(\sigma_f + \sigma_r)}{(\sigma_f - \sigma_r) - 2 * \sigma_y} \quad (2)$$

Where σ_f and σ_r represents the forward stress and reverse yield, respectively, and σ_y is the yield strength is initial yield.

In this work, we present the results of experiments performed on an extruded 6061 aluminum alloy prestrained in both tension-followed-by compression and compression-followed-by-tension. Furthermore, we capture the evolution of the BE in extruded 6061 aluminum alloys using an internal state variable plasticity and damage model. As such, to the best of the authors' knowledge, this is the first study focused on modeling and experimentally characterizing the BE in an extruded 6061 aluminum alloy.

Fatigue in Light Weight Alloys

Like many metals, the failure due to fatigue is an important aspect of material behavior and extensive testing and a crucial component of the implementation of AA6061. The fatigue performance of these aluminum alloys like most metallic materials is affected by both extrinsic factors, such as thermal environment (Lipkin, Swearengen, and Karnes 1973; Srivatsan, Sriram, and Daniels 1997; Srivatsan, Yamaguchi, and Starke 1986; Abedrabbo, Pourboghra, and Carsley 2006) and loading history (Myhr et al. 2004; Srivatsan, Sriram, and Daniels 1997; Minakawa, Levan, and McEvily 1986; L. Wang et al. 1996), and intrinsic factors including grain size and crystallographic orientations, inclusion, void formation and magnitude of damage accumulation (Chan 2010; Caton, Jones, and Allison 2001; L. Wang et al. 1996; Levin and Karlsson 1993; Shin and Huang 2010; Chen and Tokaji 2004; K Gall, Yang, and Horstemeyer 1999). The formation of fatigue damage within these materials has been well established as the coordinated progression of four distinct phases “stages”, including incubation, microstructurally small crack, physically small crack and long crack “fast fracture” growth (Suresh 1983; D. McDowell 1997a).

Of late, this paradigm has seen extensive application in a multi-scale and multi-stage microstructurally sensitive fatigue model (MSF) as its central, systematic framework (M F Horstemeyer 2010). This MSF model was originally developed to capture the fatigue behavior of cast A356-T6 based on the intrinsic structure properties of porosity, hard silicate precipitates and spatial orientations of these feature (D. . McDowell et al. 2003; Y. Xue, Burton, et al. 2007). The MSF was later extended to include other cast alloys including hexagonal close pack (HCP) oriented AE44 and AM50 magnesium (Y Xue et al. 2007; Kadiri et al. 2006). Furthermore the model was expanded to incorporate non-porosity dominated metals, such as wrought Al-Zn-Mg

aluminum alloys (AA7075) and AA6061-SiC metal matrix composites, where cracks initiated from intermetallic and reinforcing particles, homogeneously distributed throughout the matrix (Y. Xue, McDowell, et al. 2007; Yibin Xue et al. 2010; McCullough et al. 2013). In addition, the MSF model captured the performance of additive manufacturing steels, including Laser Engineered Net Shaping (LENS™)-processed 316L steel and FC-0205 steel, where large porosity created a limited, microstructurally small crack contribution to total fatigue life (Allison et al. 2013; Y. Xue et al. 2010; J. B. Jordon and Horstemeyer 2014). The MSF model was also shown to be effective in capturing the fatigue behavior of Acrylonitrile Butadiene Styrene (ABS) Copolymer and demonstrated that the multi-stage paradigm used for metallic alloys was also effective for polymers (Marcos Lugo et al. 2014).

The focus of the study presented in this project is to capture the mechanisms of multi-stage fatigue damage in Al-Mg-Si (AA6061) alloys. While a few experimental studies on the low cycle fatigue performance of AA6061 (Brammer et al. 2012; Abood, Saleh, and Abdullah 2013) exist to the best of the author's knowledge, no study has yet been performed that examines the fatigue life of AA6061 with an in-depth micromechanical study of the microstructural response of the material through fractographic analysis and finite element simulation. The MSF model was compared with experimental results to better understand the occurrence of fatigue within AA6061 and establish an improved paradigm for future material process and component design methodologies. A modified annealing treatment was utilized to introduce controlled variance in the microstructure of the as-received material to aid in the analysis of micro-mechanical performance within AA6061.

EXPERIMENTS AND MATERIALS

Material Preparation

The material used in this study is a wrought Al-1%Mg -0.7%Si aluminum alloy (AA6061) that was received from Taber Extrusion of Arkansas, USA, as extruded rail stock in T6 heat treatment condition. For mechanical testing a modified ASTM E606-92 cylindrical fatigue specimen was used that incorporated a smaller gage section and increased cross-sectional area for the purpose of eliminating the potential of buckling of the specimen during high compressive strain loadings. The gage length and diameter of the dog-bone shaped specimens were 15 mm and 8 mm respectively. All specimen gage sections were polished with 320 grit silicon carbide paper along the longitudinal axis to remove radial featured and machining defects.

From literature it has been noted that aluminum alloys, specifically AA6061, can be exposed to elevated thermal environments that significantly affect the alloy's long-term implementation during use, by reducing key mechanical properties (Prietto et al. 2011; Aizpuru et al. 2005; Wilhelm et al. 2009). Therefore in order to study the mechanical and microstructural properties of AA6061 in a thermally affected state, a specifically design heat treatment schedule was developed with characteristics similar to an annealing treatment. For this annealing process, a Carbolite ELF 11/23 box furnace was utilized to obtain a 316°C ambient air, thermal environment. The temperature exposure of the AA6061 included ramp and hold times of approximately 960 +/- 10 seconds and 440 +/-20 seconds. The interval between the heat treatment and placement on cooling rack was approximately 1 minute. The specimens were cooled at

ambient room temperature (24.4°C) for 20 minutes. An Extech SDL200 thermocouple meter calibrated to NIST standards was utilized to record ambient, local, and material reference temperatures during the annealing process. For discussion purposes in this paper, the modified annealing processed material is referred to as “annealed.”

Mechanical Characterization

Experiments Room temperature ($T = 24.4^{\circ}\text{C}$ and $H = 42\%$) fatigue tests were carried out on a MTS 809 Axial/Torsion servo-hydraulic load frame with a Flextest 40 control suite. Uniaxial monotonic testing was conducted at a strain rate of 0.001/s till failure. Reversing load tests were run at a strain rate of 0.001/s for 3.0% and 5.0% pre-strain levels in both tension-followed-by compression (T-C) and compression-followed-by-tension (C-T). Fatigue testing was conducted with a load ratio of $R=-1$. The tests were run at 1 Hz for strain amplitudes between 2.5% to 0.7% and 5 Hz for strain amplitudes, from 0.7% to 0.3%. When cycle count reached 20,000, the material was assumed to be cyclically stable and the testing was continued in load control based on the last peak/valley load reading and run at 20 Hz to final failure. Testing was stopped when the final failure of the specimen was reached, which for this study was defined as a 50% drop in peak load during the test, as recommended by ASTM Standard E.606. All strain values were measured using a MTS 634.31E-25 extensometer with a 12.7 mm gage length.

Microstructure Characterization

In order to capture the characteristics of the AA6061 microstructure of optical and electron microscopy techniques were used. All cross-sectional specimens were mounted using a cold mount resin and polished using a diamond suspension down to 0.5 microns, with final

polishing consisting of 50 nanometer colloidal silica. The samples were then ultrasonically cleaned in ethanol to remove clinging polishing particulates. An etching technique after (Mohammadtaheri 2012) was utilized in order to produce highly contrasted grain boundaries and precipitate sites. The first step was composed of pre-etching for 30 seconds in a solution of 1 g NaCl in 50 mL of H₃PO₄. Step two included etching for 6 seconds with Weck's reagent (1 g NaOH and 4 g KMnO₄ in 100 mL of H₂O). The entire etching process was conducted at room temperature and the specimens were regularly cleaned with critical detergent to remove excess solution from the etched surface.

For optical imaging, a Keyence VHX-2000 Digital microscope with a VH-Z100 lens was employed. For high magnification electron imaging, a JEOL 7000 series field emission scanning electron microscope equipped with an Oxford X-Max Silicon Drift EDS Detector was employed. For crystallographic analysis, an Oxford Scientific NordlysNano Electron Back-Scatter Diffraction device was used to measure the microstructure and grain texture of both as-received and annealed condition. Electron backscatter diffraction (EBSD) was employed to capture the change in microstructure due to the annealing schedule implemented in this study. The surface was scanned using a very low magnification to maximize the capture of a large surface area. A 2.5 micron step size and 25kv source voltage was employed. Area of analysis was 1.8 mm by 1.25 mm to capture macroscale grain distribution and maximize grain population. EBSD surface scans were taken at distances of 2 mm from the surface of the specimen to capture both subsurface and core (central) microstructure.

COMPUTATIONAL MODEL

ISV Plasticity Damage Model

An internal state variable plasticity-damage model developed by Bammann and Co-Workers (D. Bammann and Aifantis 1989) has shown good correlation in capturing the evolution of plasticity due to the response of the microstructure of ductile metallic alloys under macroscale mechanical loading. For discussion purposes, we refer to Bammann and co-Workers' internal state variable plasticity-damage model as simply the "ISV" model. To improve the ISV model's effectiveness, modifications have been made that account for microstructure damage evolution through crack and/or void nucleation and growth, as well as coalescence of voids (M. Horstemeyer and Gokhale 1999; M.F. Horstemeyer et al. 2000; Tucker et al. 2010) for types of metals, under various loading conditions (M F Horstemeyer 2001; QG Wang 2004) (M F Horstemeyer 2001; QG Wang 2004).

The ISV model itself is a physically motivated constitutive model. This model captures the Bauschinger effect through the inclusion of the kinematic and isotropic hardening and recovery components and damage (arising from cracked or debonded particles) (M. F. Horstemeyer and Ramaswamy 2000). The ISV model has been used to capture the Bauschinger effect in steel (M. Miller 1999) and in cast and rolled aluminum alloys (J.B. Jordon et al. 2007). Furthermore, the ISV model captured the stress state dependence in multiphase, fiber reinforced aluminum composite (Tang et al. 2012). Regarding AA6061, damage is primarily governed by growth and coalescence of micro voids (Agarwal and Gokhale 2003) and thus, the degradation

on the flow stress from this type of damage is explicitly captured by the ISV model. The ISV model used in this study has been correlated to experimental results using a non-linear, least-square technique fitting both strain rate and temperature dependence (Guo, Wen, and Horstemeyer 2005).

While the early versions of the ISV are described in detail elsewhere (Douglas J. Bammann 1990; D.J. Bammann et al. 1993), a complete description of the current configuration of the model is give. The kinematics of the ISV model are based on the multiplicative decomposition of the deformation gradient into elastic, plastic and damage components.

$$F = F_e F_{th} F_d F_p \quad (3)$$

As such, other kinematic quantities exists and can be defined with respect to any possible configuration via standard push forward, pull back of any of the configurations operations. To illustrate this, the velocity gradient can be decomposed into the current configuration with the following additive components:

$$L = \dot{F}F^{-1} + F_e \dot{F}_{th} F_{th}^{-1} F_e^{-1} + F_e F_{th} \dot{F}_d F_d^{-1} F_{th}^{-1} F_e^{-1} + F_e F_{th} F_d \dot{F}_p F_p^{-1} F_d^{-1} F_{th}^{-1} F_e^{-1} \quad (4)$$

where, $L_e = \dot{F}_e F_e^{-1}$ is the elastic velocity gradient defined with respect to the current configuration, $\widetilde{L}_d = \dot{F}_d F_d^{-1}$ is the velocity gradient associated with damage and is defined with respect to the configuration F_d , while $L_p = \dot{F}_p F_p^{-1}$ is the plastic velocity gradient residing in the configuration defined with respect to F_p . It is important to note that total strain or velocity gradient is simply the sum of the elastic damage and plastic parts, where each is defined by the appropriate pull-back operation. As such, the ISV model is defined with respect to F_p the configuration, which is the configuration that is reached by the unloading through the elastic and damage configurations. Next, the Helmholtz free energy is described as a function of the elastic strain, where it is assumed that the free energy takes the form of a quadratic function of the

elastic strain. This leads to the Hooke's law formulation, which after taking the material derivative and pushing forward to the current configuration, produces an expression for the linear elasticity in the current configuration. The Cauchy stress equation, shown in Equation 5, describes total deformation (D), where Equation 6 expresses the elastic deformation (D^e) in terms of total and elastic components.

$$\dot{\sigma} = \lambda(1 - D)tr(D^e)U + 2\mu(1 - D)D^e - \frac{\dot{D}}{1-D}\sigma \quad (5)$$

$$D^e = D - D_d^p \quad (6)$$

The flow stress rule (D_d^p), is described in terms of deviatoric Cauchy stress (σ') and the tensor variable (α'):

$$D_d^p = \sqrt{\frac{3}{2}}f(T) \sinh \left[\frac{|\sigma' - \alpha| - \{R + Y(T)\}(1 - \phi)}{V(T)(1 - \phi)} \right] \frac{\sigma' - \alpha}{|\sigma' - \alpha|} \quad (7)$$

Where the kinematic (α) and isotropic (R) internal state variables are given in Equation 8 and 9, respectively. As represented in these equations, the evolution of the kinematic and isotropic internal state variables is described by a hardening minus recovery component. The capturing of the BE by the ISV model is largely related to the hardening minus recovery formulation. In fact the internal state variables are motivated by dislocation mechanics. The isotropic hardening internal state variable is motivated by statistically stored dislocations (SSD) densities that are typically created and stored in the grain. On the other hand, the kinematic hardening internal state variable is motivated by what is known as geometrically necessary dislocations (GND). These dislocations exist to restore the compatibility at the grain boundaries. Dislocations of the same sign that accumulate against a boundary are also represented as GNDs and their motion under load reversal gives rise to an apparent softening or a BE.

$$\dot{\alpha} = \left[h(T)D^p - \left(\sqrt{\frac{2}{3}}r_d(T)\|D^p\| + r_s(T) \right) \|\alpha\|\alpha \right] \left[\frac{GS_0}{GS} \right]^Z \quad (8)$$

$$\dot{R} = \left[H(T) \|D^p\| - \left(\sqrt{\frac{2}{3}} R_d(T) \|D^p\| + R_s(T) \right) R^2 \right] \left(\frac{GS_0}{GS} \right)^Z \quad (9)$$

The evolution of damage is described by a damage parameter, ϕ , where the deformation (\dot{D}) as a function of void nucleation, growth, and coalescence, with equations 10-13 representing the constitutive components for particle sourced void ($\dot{\phi}_{\text{particle}}$) nucleation rate ($\dot{\eta}$) and growth rate ($\dot{\nu}$), as well as growth from pre-existing void growth rate ($\dot{\phi}_{\text{pore}}$) and void coalescence rate (\dot{c}) (M. Horstemeyer and Gokhale 1999).

$$\dot{D} = [\dot{\phi}_{\text{particles}} + \dot{\phi}_{\text{pores}}]C + [\phi_{\text{particles}} + \phi_{\text{pores}}]\dot{C} \quad (10)$$

$$\dot{\phi}_{\text{particles}} = \dot{\eta}\nu + \eta\dot{\nu} \quad (11)$$

$$\dot{\eta} = \|D^p\| \left\{ \frac{(a^{1/2})}{K_{IC}f^{1/3}} \eta \left\{ a \left[\frac{4}{27} - \frac{J_3^2}{J_2^3} \right] + b \frac{J_3}{J_2^{3/2}} + c \left\| \frac{I_1}{\sqrt{J_2}} \right\| \right\} \right\} \exp\left(-\frac{C\eta T}{T}\right) \quad (12)$$

$$\dot{\nu} = \frac{\sqrt{3}R_0}{2*(1-n)} \left[\sinh\left(\frac{\sqrt{3}(1-n)(\sqrt{2}I_1)}{2\sqrt{J_2}}\right) \right] \|D^p\| \quad (13)$$

$$\dot{c} = C_{\text{coal}}[\eta\dot{\nu} + \dot{\eta}\nu] \exp(C_{CT}T) \left(\frac{GS_0}{GS} \right)^Z \quad (14)$$

$$\dot{\phi}_{\text{pores}} = \left[\frac{1}{(1-\phi_{\text{pores}})^m} - (1 - \phi_{\text{pores}}) \right] * \sinh\left\{ \frac{2*(2V(T)/Y(T)-1)}{(2V(T)/Y(T)+1)} \left(\frac{\sigma_H}{\sigma_{vm}} \right) \right\} \|D^p\| \quad (15)$$

The damage equations capture the nucleation in terms of de-cohesion of the material matrix or particle fracture. In addition, the model allows void growth to occur at different sides of the cracked or de-bonded particle with the size of the newly initiated void assumed to be the size of a second phase particle. Finally, the void coalescence is added to the model to capture the event of multiple voids growing together and joining and eventually resulting in ductile failure.

The model parameters V , Y , H , R_d , R_s , h , r_d , r_s , are functions of temperature, stress state and strain rate and are correlated from experiments, as shown in Table 1, where $J'_2 = \frac{1}{2(\sigma' - \alpha)^2}$,

$$J'_3 = \frac{1}{3(\sigma' - \alpha)^3} \text{ and deviatoric stress tensor } \sigma'_{ij} = \left(\sigma_{ij} - \frac{1}{3}\sigma_{kk} \delta_{ij} \right).$$

Table 1. Relationship functions for ISV plasticity model

	Equation	Unit
Magnitude of Rate Sensitivity	$V(T) = C_1 e^{-\frac{C_2}{T}}$	MPa
Rate-Dependent Yield Stress	$Y(T) = C_3 e^{-\frac{C_4}{T}}$	MPa
Rate-Sensitivity Impact on Yield Stress	$f(T) = C_5 e^{-\frac{C_6}{T}}$	1/S
Anisotropic (Kinematic) Dynamic Recovery	$r_d(T) = C_7 e^{-\frac{C_8}{T}}$	1/MPa
Anisotropic (Kinematic) Hardening Modulus	$h(T) = C_9 e^{-\frac{C_{10}}{T}}$	MPa
Anisotropic (Kinematic) Diffusion-controlled Static Recovery	$r_s(T) = C_{11} e^{-\frac{C_{12}}{T}}$	1/(MPa*S)
Isotropic Dynamic Recovery	$R_d(T) = C_{13} e^{-\frac{C_{14}}{T}}$	1/MPa
Isotropic Hardening Modulus	$H(T) = C_{15} e^{-\frac{C_{16}}{T}}$	MPa
Isotropic Diffusion-controlled Static Recovery	$R_s(T) = C_{17} e^{-\frac{C_{18}}{T}}$	MPa/S

Multi-Stage Fatigue Model

Stages of Fatigue Damage

Proposed by McDowell et al (D. McDowell 1997a; D. McDowell 1997b) to analyze the fatigue performance of a cast aluminum alloy A356, the MSF model has since been adapted and expanded by a range of contributors, in order to model a wide range of material systems engineered through the use of various methodologies (Y. Xue, McDowell, et al. 2007; J.B. Jordon et al. 2011; J B Jordon, Gibson, and Horstemeyer 2011; Allison et al. 2013; Rettberg et al. 2012; M. Lugo et al. 2013). The multi-stage approach of the following experimentally observed stages of fatigue damage: (i) crack incubation, (ii) growth of micro structurally small crack (MSC), (iii) growth of physically small crack (PSC), and (iv) long crack growth. The summation of these results in the total number of cycles to failure given by:

$$N_{total} = N_{inc} + N_{\frac{MSC}{PSC}} + N_{LC} \quad (16)$$

Where N_{inc} represents the incubation life contribution in number of cycles of a crack incubated at the root of a microscopic notch, assumed to compose of two phases: first, the nucleation of a crack-like defect, and second, the early stages of propagation of the defect through the influence zone at the tip/root of the microscopic notch. The $N_{MSC/PSC}$ is the sum total of the two stages composing of the development of small cracks out of the micro-notch root influence zone and up to a physically significant scale. N_{MSC} represents the number of cycles required for propagation of a microstructurally small crack; N_{PSC} is the number of cycles required for propagation of a physically small crack (PSC). The final stage of crack propagation is represented by N_{LC} , which is the number of cycles required for propagation of the long crack to final failure.

Crack initiation (INC) essentially involves crack nucleation, plus a minimal level of small crack growth at the root of a microscopic notch, such as formed at an inclusion (a_i). This small crack is assumed to be on the order of one-half the diameter of the sourced inclusion. Small crack growth (MSC) comprises the propagation of microstructurally small cracks having a length range of a_i , with $a_i < a < k$ (MS). In this expression, the MS is the characteristic length scale of interaction with the concerned microstructural (MS) feature, often, the smallest grain size, and k is a constant and in the range between one and three. The range of a physically small crack (PSC) consists of propagation of the crack in the interval k (MS) $< a < O$ (10 MS). The magnitude of the PSC depends on both morphology of the microstructural inclusion, and texture of the matrix. Due to these synergistic effects, the regime of PSC can extend anywhere from 300 μm to 2-3 mm in length.

Crack Incubation

As shown in equation 1, the initial phase of crack incubation is the number of cycles (N_{inc}) till the onset of fatigue crack. There, incubation of a crack within the microstructure of the material is characterized by the incident of microscopic notch centric, cyclic fatigue damage. To capture the onset of this damage at the root of the micro-notch, the model employs a modified Coffin-Manson law optimized for micro scale interactions.

$$C_{inc} N_{inc}^{\alpha} = \frac{\Delta\gamma_{max}^{p^*}}{2} = \beta = \psi \bar{Y} [\varepsilon_a - \varepsilon_{th}]^q \quad (17)$$

In Equation 17, C_{inc} and α represent the linear and exponential (D. . McDowell et al. 2003) coefficients in the modified Coffin-Manson law for crack incubation, β represents a nonlocal parameter that defines the damage around an inclusion. $\frac{\Delta\gamma_{max}^{p^*}}{2}$ is the local average maximum plastic shear strain amplitude. ε_a is the remote applied strain amplitude and ε_{th} is the

microplasticity strain threshold. The localized plastic region developed around an inclusion is expressed by the ratio l/D , where D is the size of the inclusion at which the initiation of a fatigue crack is favored to occur and l represents the nominal linear dimension of the plastic zone generated in front of the inclusion. Simplified, the ratio l/D can be defined as the square root of the ratio of area of the developed plastic zone to total area of the suspended inclusion.

The final segment of the incubation portion of the MSF model is focused on the evolution of the strain field away from the inclusion. The plasticity field that develops at the root of the micro-notch eventually saturates and the limiting ratio (η_{lim}), indicates the transition from the initial state of constrained plasticity to unconstrained (non-linear) plasticity under the influence of the remote applied strain amplitude (J.B. Jordon et al. 2011). To correlate the development of local plastic shear strain to remote applied strain, the parameter Y is taken to be $\bar{Y} = Y = y_1 + (1 + R) * y_2$, where R is the load ratio, and y_1 and y_2 are model constants related to remote applied strain translation local plastic shear strain. Furthermore, when l/d reaches its limit ($\eta_{lim} < \frac{l}{D} \leq 1$), the parameter \bar{Y} is modified to include the geometric effect, $\bar{Y} = (1 + \zeta * \frac{l}{D}) Y$.

The term ψ is a relationship that integrates experimentally observed microstructure properties into the incubation parameter, which increases model sensitivity to variance microstructure. This expression $\left[\frac{(MPS^2)}{(NND)(GS)} \right]^\gamma$, is a function of namely the maximum particle size (MPS), nearest neighbor distance (NND) and grain size (GS), as well as γ , a sensitivity exponent (J.B. Jordon et al. 2009). As stated previously, l/D is an expression that defines the local plastic zone, which in turn is correlated to remote strain. The correlation of the size of the plastic zone with respect to remote strain amplitude is calculated using the nonlocal plastic shear strain:

$$\frac{l}{D} = \eta_{lim} \frac{\langle \varepsilon_a - \varepsilon_{th} \rangle}{\varepsilon_{per} - \varepsilon_{th}}, \quad \frac{l}{D} \leq \eta_{lim} \quad (18)$$

$$\frac{l}{D} = 1 - (1 - \eta_{lim}) \left(\frac{\varepsilon_{per}}{\varepsilon_a} \right)^r, \quad \frac{l}{D} > \eta_{lim} \quad (19)$$

In this expression, r is the shape constant for the transition to limited plasticity (Hayhurst, Leckie, and McDow 1985; Brown et al. 2007). In this study, the microplasticity constants representing the strain threshold ε_{th} and percolation limits ε_{per} , were determined through micromechanical simulations. It has also been seen in literature (Y. Xue, McDowell, et al. 2007) that these two values can also be captured using standard endurance limit calculations, where $\varepsilon_{th} = \frac{0.29S_{ut}}{E}$ and $\varepsilon_{per} = \frac{0.7\sigma_y^{cyclic}}{E}$ respectively and S_{ut} is ultimate tensile strength, σ_y^{cyclic} is the stabilized cyclic yield strength and E is the elastic modulus.

Small Crack

Once the localized plastic zone has saturated, the crack begins to travel through the material matrix, forming the next phase of fatigue damage. In MSF, this growth is modeled through the concept of crack tip displacement (ΔCTD), which is used to account for growth in both the microstructurally small and physically small crack regimes. The term ΔCTD can be expressed to account for varying degrees of contribution of high cycle fatigue (ii) and low cycle fatigue (i) regimes, depending on the remotely applied strain amplitude. In high cycle fatigue the crack tip displacement is correlated to the length of the crack and the applied stress amplitude (σ_a). Subsequently in low cycle fatigue, CTD is proportional to the macroscopic shear strain range. Equation 20 represents the governing crack growth law as a function of CTD:

$$\left(\frac{da}{dN} \right)_{MSC} = \chi (\Delta CTD - \Delta CTD_{th}), \quad a_i = 0.625D \quad (20)$$

Where χ is a constant related to the crack propagation rate within the microstructure, which is of the range between zero and unity typically residing between .33 and .5. For aluminum alloys this value has been taken to be 0.35 (D. . McDowell et al. 2003). Burger's vector for pure FCC aluminum ($\Delta CTD_{th}=2.85*10^{-4} \mu m$) was used to define the threshold value for crack tip displacement. The a_i is the initial crack length as a function of inclusion size. Equation 6 defines ΔCTD as a function of remote applied loading:

$$\Delta CTD = C_{II} \Psi \left(\frac{GS}{GS_0} \right)^\omega \left[\frac{U \Delta \hat{\sigma}}{S_{ut}} \right]^\zeta a_i + C_I \Psi \left(\frac{GS}{GS_0} \right)^\omega \left(\frac{\Delta \gamma_{max}^p}{2} \right)^2 \quad (21)$$

Where the constants C_I and C_{II} are material dependent parameters for capturing the effects of microstructure on the microstructurally small crack growth in low cycle and high cycle fatigue regimes respectively. The term $\Delta \hat{\sigma}$ is given as $\Delta \hat{\sigma} = 2\theta \bar{\sigma}_a + (1 - \theta) \Delta \sigma_1$, where $\bar{\sigma}_a$ is the uniaxial effective stress amplitude $\left(\sqrt{\frac{3}{2} \frac{\Delta \sigma'_{ij}}{2} \frac{\Delta \sigma'_{ij}}{2}} \right)$, $\Delta \sigma_1$ is the maximum principal stress range and θ is the path dependent loading parameter (Kumai, King, and Knott 1990), where $0 \leq \theta \leq 1$. The effect of loading ratio is account for in the parameter $U = \frac{1}{1-R}$. The ΔCTD equation is also sensitive to the effect of grain size on small crack growth through the ratio $\left(\frac{GOS}{GOS_0} \right)^\omega$, where GS_0 is the reference grain size, GS is the specific grain size, and ω is a material constant (Y. Xue, McDowell, et al. 2007).

Long Crack

The MSF model can capture damage from long crack growth through classical linear elastic fracture mechanics approach or be coupled with more complex fracture mechanics models like Fastran (Newman 1995). However, while long crack growth is an integral part of failure, the

contribution of long crack to fatigue life is limited in ductile metals, such as aluminums, as it typically occurs at millimeter length scales within the material (D. . McDowell et al. 2003). Therefore, the MSF model in the scope of this study will only be utilized to account for the incubation and small crack stages of fatigue in conformance with literature (Rettberg et al. 2012; J.B. Jordon et al. 2011; J.B. Jordon et al. 2009), where these two stages represent the vast majority of failure cycles in fatigue.

RESULTS AND DISCUSSION

Microstructure

Chemically etched optical micrographs of the AA6061 material are shown in Figure 2 in the as-received (Fig. 2a) and annealed condition (Fig. 2b). The etching assisted in the definition of the intermetallic particles suspended within the matrix. The dominant grain shape in both conditions was observed to be semi-circular, with only a small variance observed in the evolution of the grain size due to the annealing schedule. While the EBSD analysis showed a large variation of grains sizes across the material cross-section, Figure 3 shows representative scans of the grains present along the center-line of the extrusion.

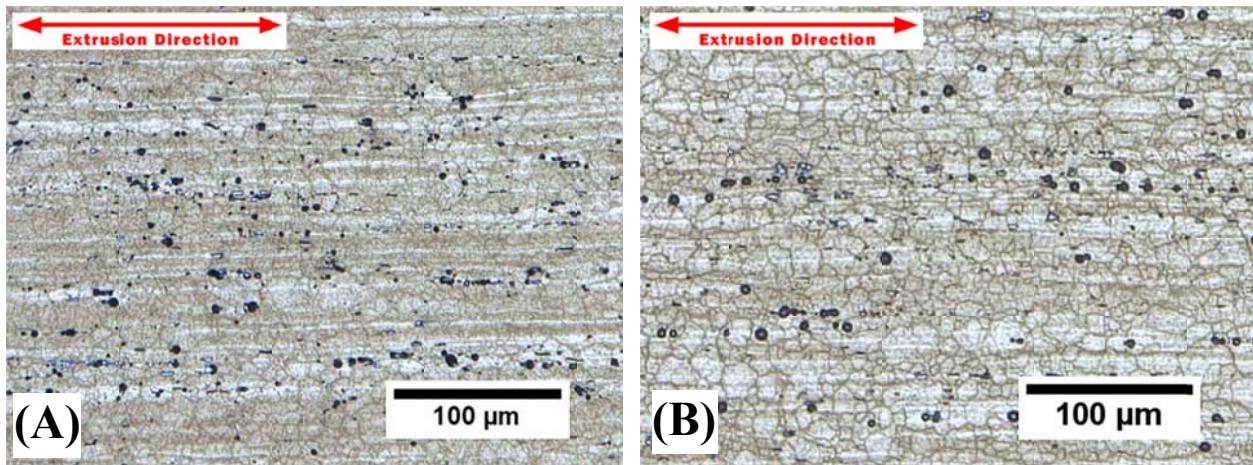


Figure 2. Optical images of etched AA6061 in (A) as-received and (B) annealed states.

In both conditions, the microstructure consisted of a majority of grains that were aligned along the extrusion direction. The mean size of the small grains for as-received condition was 7.5 μm and 9 μm for the annealed condition. While not shown, very large grains were observed to be

scattered intermittently in both materials, with some grains measured as large 500 μm . This bimodal grain distribution observed in this study is consistent with post-extrusion heat treatment that produces sequential layering between round and pancake shaped grains (Kliauga and Ferrante 2005) and in other similar wrought Al-Si-Mg alloys (K. O. Pedersen et al. 2008).

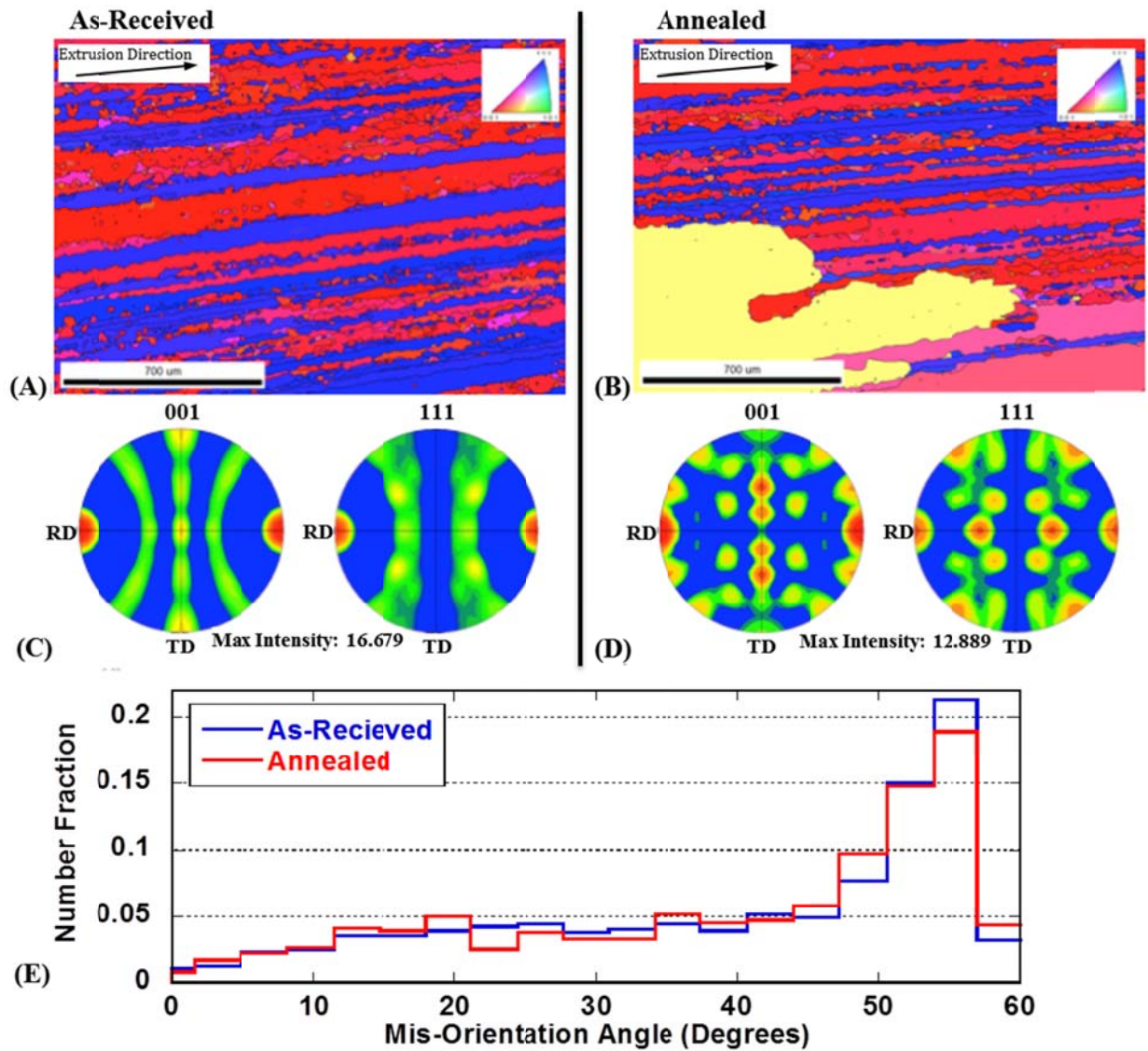


Figure 3. Electron backscatter diffraction results for 6061 aluminum alloy with IPF charts oriented in the extruded direction (A and B), pole figure (C and D), and the misorientation angle chart (E).

Particles were found to be distributed through the matrix in a non-uniform pattern of stringers oriented in the extrusion direction, as observed in a similar wrought alloy (K. O. Pedersen et al. 2008; Schikorra et al. 2007). In addition, there were regions of very low concentrations of intermetallic particles. This distribution pattern is consistent with observations reported elsewhere (Mrówka-Nowotnik 2010). Similar to the annealing on the grain structure, no significant difference was found in the size or distribution of the intermetallic particles between the as-received and annealed materials. EDX analysis revealed the presence of iron-silicon rich intermetallic particles distributed throughout the matrix in both the as-received and annealed conditions, as shown in Figure 4. Based on results of elemental ratios from the EDS measurements, the primary composition of the most prominent particle was Fe_2SiAl_9 , with $\text{Fe}_3\text{SiAl}_{12}$ and Mn-rich intermetallic particles also present, however, their concentration was much lower than that of Fe_2SiAl_9 particles. The size of Fe_2SiAl_9 particle was on the order of several microns with the mean diameter of $1.5\ \mu\text{m}$ in the as-received and $1.8\ \mu\text{m}$ for the annealed condition. The aspect ratio for Fe_2SiAl_9 particle was approximately 2.3 with a volume fraction range of 1.69% to 2.3% for both materials.

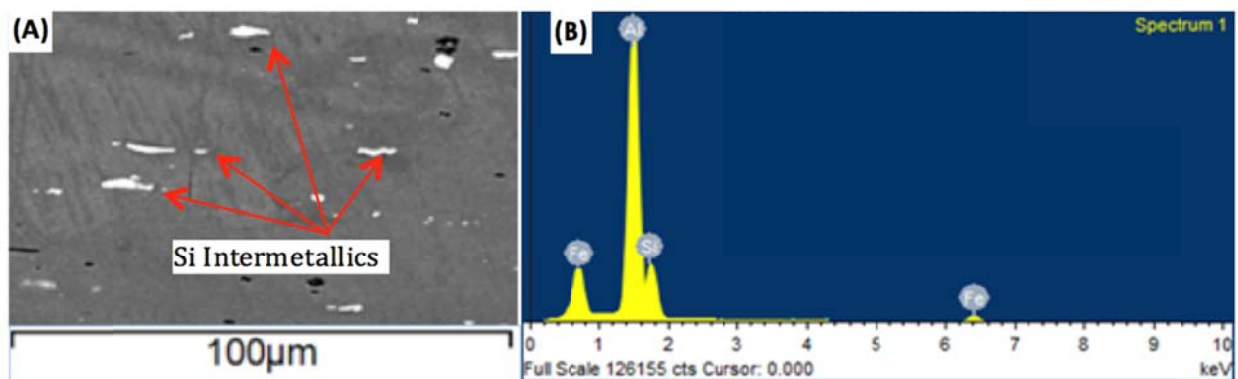


Figure 4. Micrograph (A) of observed Ferrite-rich, Silicon-based intermetallic particles and the corresponding chemical analysis (B).

Monotonic and Cyclic Stress/Strain Response

As expected, tensile test results of both AA6061 materials exhibited high levels of work hardening due to the extrusion process, as shown in Figure 5. The AA6061 material did show a significant softening from the annealing process, which was correlated to the slight recrystallization during treatment observed from optical microscopy. In addition to the tensile stress-strain curves, the cyclic stress strain curves are also shown. Only slight differences were noted in the elastic behavior of both materials, noted by the slight differences seen the calculated elastic moduli from Table 2. The effect was more pronounced for the yield and ultimate strengths, where the difference was noted to decrease by 11% and 9% from the as-received and annealed materials, respectively. The cyclic regime was seen to experience similar traits, with the yield strength and hardening behavior both being significantly reduced. This was concluded to be due to the effects of material softening during annealing. Both materials were noted as still experiencing mixed hardening behavior under cyclic loading with both the annealed and as-received materials showing a slight amount of cyclic hardening during loading.

Table 2. Monotonic tensile properties of 6061 aluminum alloy

	As-Received	Annealed	
Modulus of Elasticity	66.4	67.5	GPa
Yield Strength	304.4	270.3	MPa
Ultimate Strength	320.8	292.5	MPa
Elongation to Failure (Gage Length: 25.4 mm)	20.0%	22.7%	
Monotonic Strain Hardening Coefficient	377.4	355.4	MPa
Monotonic Strain Hardening Exponent	0.039	0.050	

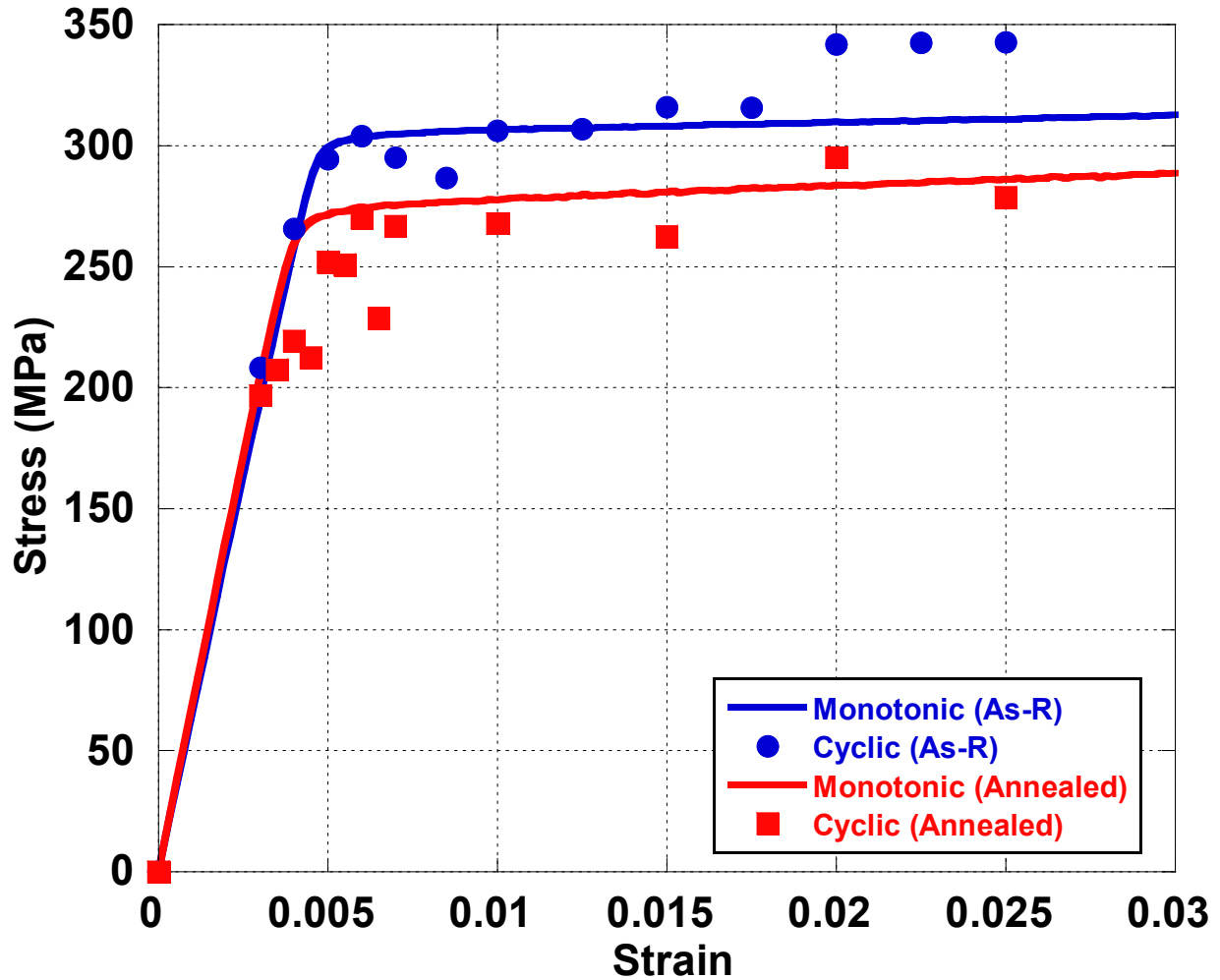


Figure 5. Monotonic and Cyclic Stress/Strain Plot.

Mechanical Evaluation of the Bauschinger Effect

Mechanical testing showed several trends in the development of plasticity in AA6061. Tensile tests on the as-received material revealed a yield strength and ductility similar to published values (Srivatsan et al. 2002; Mrówka-Nowotnik 2010), while the annealed showed an 11% decrease in yield strength and a 14% increase in ductility. In addition, a softening in the ultimate strength response can be clearly noted in the AA6061 material, after the annealing process. Table 3 presents the results of the mechanical testing.

Table 3. Bauschinger effect results by prestrain for AA6061 aluminum alloy

Prestrain	Direction	Sy (MPa)	Sr (MPa)	Sf (MPa)	a	R	BSP	RKI
<i>As-Received</i>								
1%	Ten-Comp	307.6	260.5	320.0	290.2	277.8	0.19	2.39
2%	Ten-Comp	307.6	211.8	323.8	267.8	251.6	0.35	3.46
3%	Ten-Comp	307.6	197.9	314.9	256.4	249.1	0.37	7.95
5%	Ten-Comp	307.6	211.2	341.6	276.4	242.4	0.38	1.92
3%	Comp-Ten	294.0	183.0	316.6	249.8	227.2	0.42	2.95
5%	Comp-Ten	294.0	209.7	329.3	269.5	234.2	0.36	1.69
<i>Annealed</i>								
1%	Ten-Comp	257.6	180.4	273.4	226.9	211.1	0.34	2.95
2%	Ten-Comp	257.6	163.8	281.1	222.4	199.0	0.51	2.50
3%	Ten-Comp	257.6	156.6	284.1	220.4	193.9	0.45	2.41
5%	Ten-Comp	257.6	117.4	254.8	186.1	188.9	0.49	2.78
3%	Comp-Ten	251.5	171.2	284.6	227.9	194.8	0.40	1.71
5%	Comp-Ten	251.5	166.8	287.4	227.1	191.2	0.42	1.68

The BSP and RKI values were calculated for all three sets of AA6061 materials and shown in Table 4. These calculations were done for both the tension-followed-by-compression and compression-followed-by-tension using the 0.2% strain offset yield definition. Figures 6a and 6b show both the RKI and BSP values plotted against applied prestrain in tension and compression respectively. It can be clearly observed that the T-C loading exhibited higher RKI and BSP values compared to the C-T loading. This strongly suggests that a larger anisotropic hardening occurred during initial compression, decreasing the reversing yield strength of both materials. This behavior was also seen in that as the prestrain increased, the overall trend for the RKI and BSP for both conditions increased. This observed trend suggests that the kinematic hardening in the material occurred at a faster rate than isotropic hardening.

Table 4. ISV model plasticity and damage constants

	Constants	As-Received	Annealed	
Constants for J/B formulas	G	24768.7	25179.1	MPa
	Bulk	69145.8	70291.7	MPa
Specifies the yield stress	C3	170	120	MPa
	C3	170	120	MPa
	C5	0.00001	0.00001	1/MPa
Kinematic hardening and recovery	C7	2.5	2.5	1/MPa
	C9	3000	3000	MPa
Isotropic hardening and recovery	C13	0.35	0.4	1/MPa
	C15	600	1200	MPa
Hardening and recovery	Ca	0	0	
	Cb	0	-0.05	
Temperature	Init. Temp	298	298	K
	Heat Gen. Coeff.	0.34	0.34	
McClintock void growth	Void Growth Exp	0.3	0.3	
	Init. Radius	0.0093185	0.0093185	Mm
<u>Dynamic Recovery</u>				
Long Range Isotropic	c21	0	0	
Long Range Kinematic	c23	50000	35000	
Long Range Kinematic Static	c25	0	0	

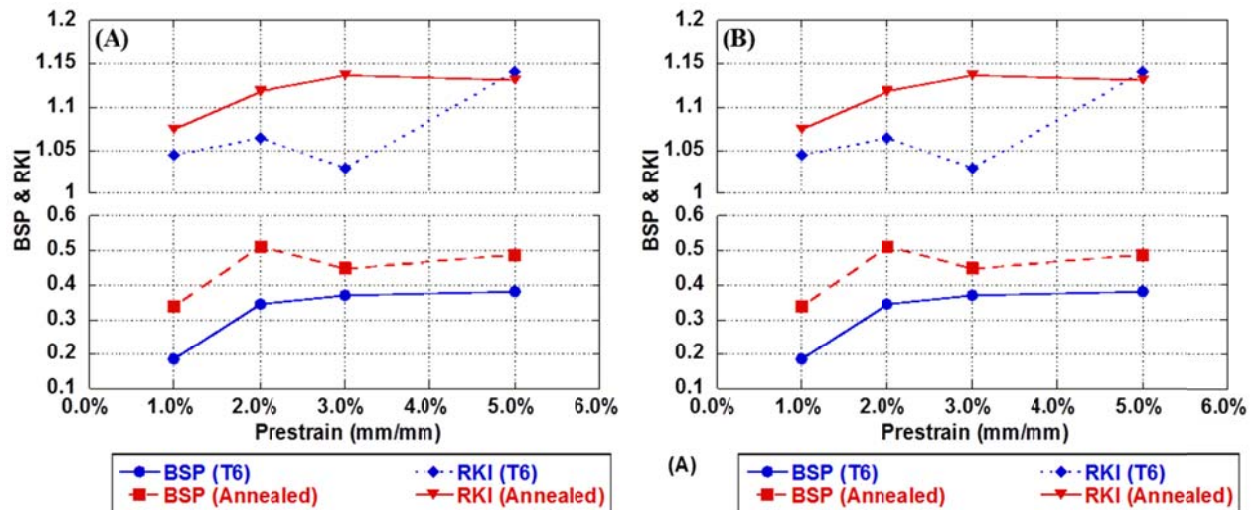


Figure 6. BSP and RKI ratio plotted versus applied forward prestrain in (A) tension-followed-by-compression and (B) compression-followed-by-tension.

This faster kinematic hardening rate is counter to current understanding of plastic flow in ductile metallic alloys. In fact, it is known that the face centered cubic (FCC) aluminum structure readily develops cross-slip mechanisms, which allows for the elimination of dislocation pileup upon reverse straining. However, due to the high stacking fault energy of aluminum, it is hypothesized that hardening is developed from dislocation pinning at secondary particles (precipitates) in the material (Embury 1987). As the dislocation density builds and reaches saturation with increasing pre-strain, reverse stress decreased due to build-up of localized strain around these precipitates and localized stress relaxation due to interface debonding and/or fracture (Choi, Barlat, and Liu 2001; Corbin, Wilkinson, and Embury 1996; QG Wang 2004; Gracio et al. 2004; Rauch et al. 2002). The buildup of damage through this mechanism continued to reduce the back-stress and increase the observed Bauschinger effect as observed by the RKI.

A key component of this ISV model is the integration of damage evolution due to void nucleation, void growth, and void coalescence. For this study, void nucleation versus applied strain was correlated to previous study (J.B. Jordon et al. 2007) of AA7075-T651 since both materials contain very similar second phases in regards to size, composition, and distribution. In fact, the AA6061 material showed similar particle fracture and interface debonding behavior in the iron-rich second phase precipitants, which in AA7075 were observed to be the main sources of void nucleation. As such, the constants for the damage equations were selected to produce the best fit of experimental monotonic tension and compression experiments. The difference observed between the tension and compression prestrain is due to the relationship of the damage nucleation difference coupled with the hardening rate difference. The local dislocation density that built up at particles relaxed as particles cracked or debonded in turn affecting the work hardening rate in the matrix. An example of the observed particle fracture is shown in Figure 7.

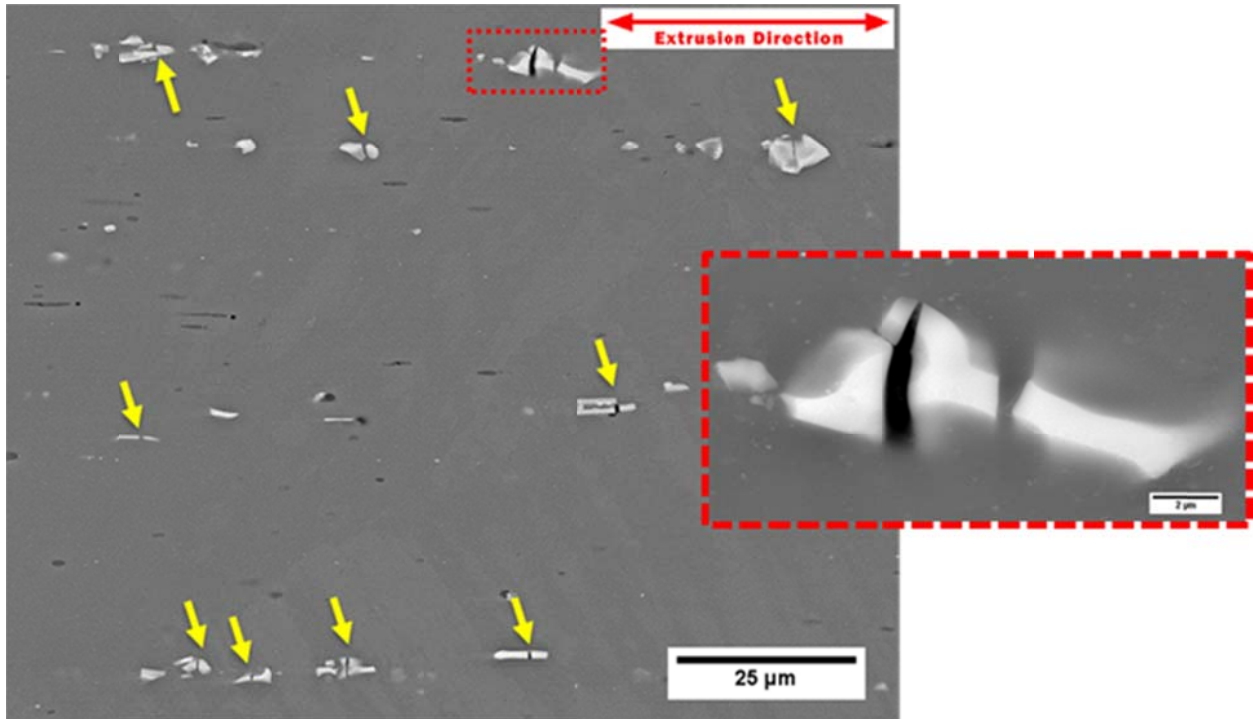


Figure 7. Fractured particles after 5% pre-strain in compression-followed-by-tension.

Taking into account both a universal set of fitted hardening and damage constants, the model was able to capture the behavior of the AA6061 alloy material in both as-received T6 heat treatment and annealed condition, as shown in Figure 8. The bulk and shear moduli were derived directly from experimental data for both states. Isotropic hardening values (c_{12} & c_{15}) were used to capture the evolution of symmetric flow stress within the materials. Dynamic kinematic recovery coefficient was used to capture the change in dislocation movement due to applied strain within the materials. The annealed material was observed to have a lower dynamic recovery rate (c_{25}), which was attributed to recrystallization within the grains and early stage solutionizing of the alloying components within the matrix during annealing. Table 5 lists the ISV model constants.

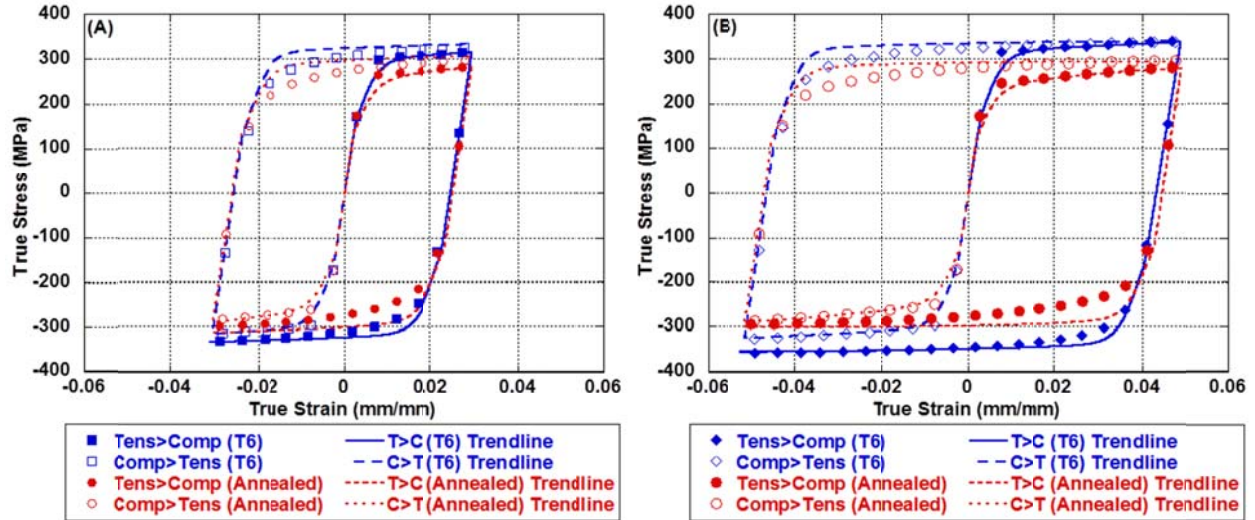


Figure 8. ISV model correlation to experimental results at (A) 3% pre-strain and (B) 5% pre-strain in tension-followed-by compression and compression-followed-by tension.

Table 5. Monotonic tensile/microstructure properties

		As-Received	Annealed	% Change	
Modulus of Elasticity	E	66.38	67.5	2%	GPa
Yield Strength	S_y	304.4	270.3	-11%	MPa
Ultimate Strength	S_u	320.8	292.5	-9%	MPa
Elongation to Failure		19.95%	22.7%	14%	

Experimental Fatigue Response

Figure 9 shows the fully-reversing, strain controlled fatigue results for the as-received and annealed materials for all collected strain levels. The fatigue behavior of AA6061 was observed to change slightly between high cycle (≤ 0.7 mm/mm) and low cycle (> 0.7 mm/mm) regions. The application of both annealed states showed little change in the performance of the annealed material versus the as-received state. However, it is noted that the annealed states appeared to exhibit slightly improved LCF performance of the material with annealing. This was attributed to the relaxation of pinned dislocations due to the annealing.

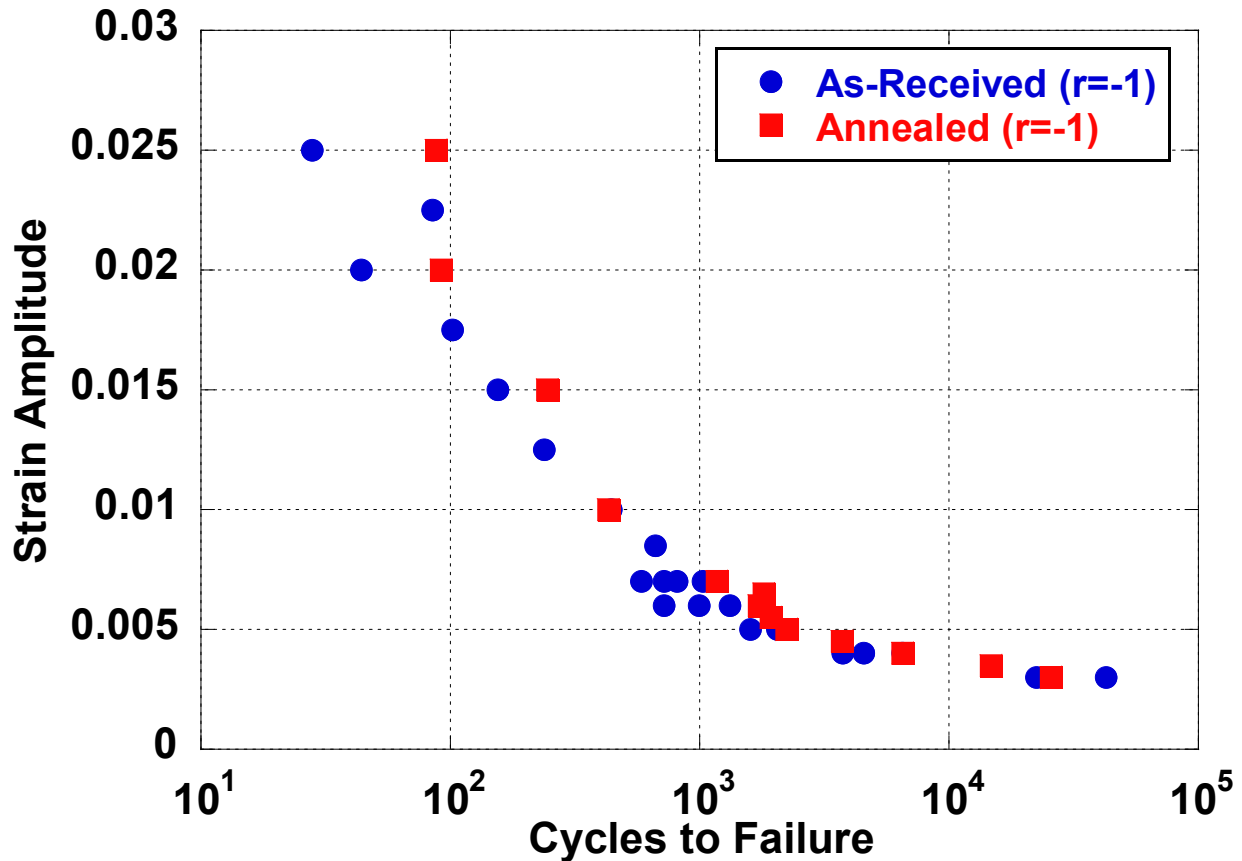


Figure 9. Strain amplitude plot of fully reversing fatigue data from as-received and annealed states.

As noted for monotonic loading, the annealed aluminum alloy showed lower stress responses under cyclic loading. Figure 10a shows the first cycle hysteresis loops for both states of AA6061. These loops were mostly symmetrical without any significant asymmetry commonly attributed to the Bauschinger effect. This trend was also seen in the stabilized (half-life) hysteresis loops (Figure 10b). A slight degree of strain hardening was observed by a slighter sharper “knee” versus the first cycle loops indicating an increased cyclic yielding point. Figure 11 shows the stress life results for the AA6061 material. It was noted that while a degree of strain hardening can be seen in the earliest stages (<10 cycles) of loading, the mechanical behavior of the AA6061 predominantly exhibited work softening, which continues till final

failure. This behavior was also observed in the annealed AA6061. Cyclic Fatigue and strain-hardening parameters were taken from this experimental data and placed in Table 6.

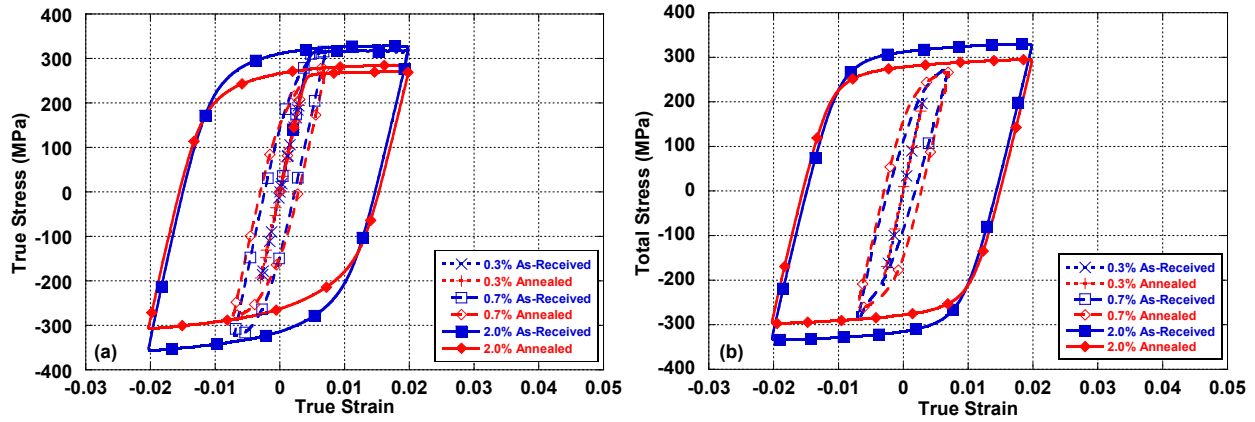


Figure 10. First cycle (a) and half-life (b) hysteresis loop plots for as-received and annealed states.

Table 6. Cyclic/fatigue parameters

		As-Received	Annealed	
Cyclic Strain-Hardening Coefficient	K'	392.8	390.2	MPa
Cyclic Strength Exponent	n'	0.044	0.0761	
Fatigue Strength Coefficient	Σf	458.0	384.6	MPa
Fatigue Strength Exponent	B	-0.063	-0.090	
Fatigue Ductility Coefficient	E_f	0.62	.6002	
Fatigue Ductility Exponent	C	-0.75	-0.757	

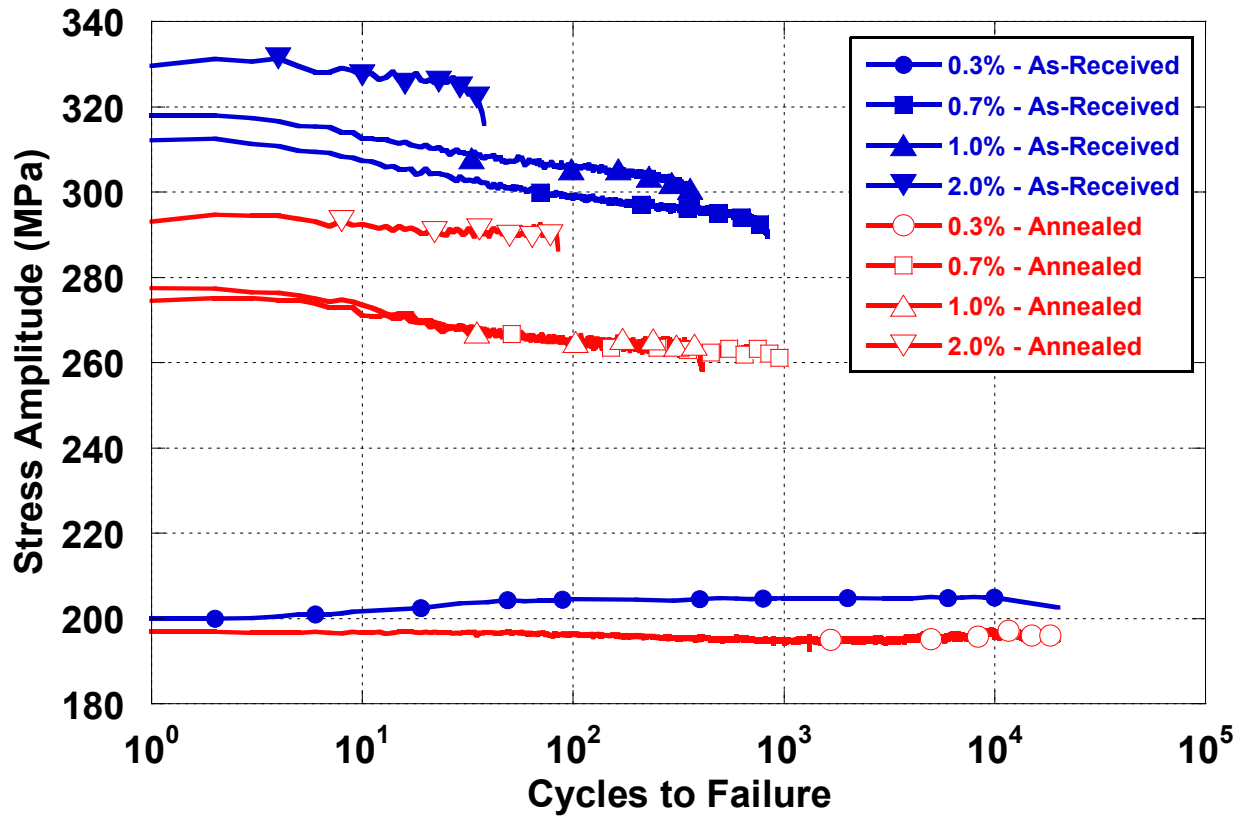


Figure 11. Fatigue life plot for as-received and annealed states.

Fractography

During a typical fatigue damage process, three distinct stages of damage occur; (incubation, crack growth & final fast fracture). Fatigue crack incubation has been seen to readily initiate near surface and/or at hard secondary phases and void-like features, such as the iron-rich inter-metallic particles commonly found in aluminum alloys (Russell and Lee 2005; Agarwal and Gokhale 2003). Once nucleated, the shear fracture mode formed the dominate failure mode, with the material developing angles of between 35-55 degrees from the load axis. This failure mode was particularly evident in high strain amplitude and load ratio testing.

SEM-based Fractography analysis was performed on various strain amplitudes in order to capture the contribution of these microstructure features. All three stages of failure were readily

observed across the range of applied loads. It was observed throughout is that most cracks incubated at sites nearby or at near-surface particles [Figures 12.a. (II) & 12.b. (IV)]. This trend was also noted in the annealed material [Figures 13.a. (II) & 13.b. (IV)]. In addition, it was observed that cracks incubated at cluster arrangements of particles in or near surface [Figure 12.b. (III) & 13.b. (III)]. The size of the particles that incubated the fatigue crack were in the mean particle size of 4-12 microns.

After incubation, crack propagation was noted to be dominated by characteristic microscopic striations. Striations were seen at nanoscale resolutions near incubation sites particles [Figures 12.a. (II) & 13.b. (IV)]. These striations were seen to then propagate from these points following a crescent shaped alignment as they moved into the interior of the material. Secondary crack coalescence with the critical crack path was also noted [Figure 12.a. (I) & 13.a. (I)]. All specimens were seen to exhibit brittle/ductile behavior outside of the striation zone, which was attributed to tensile overloading at final failure.

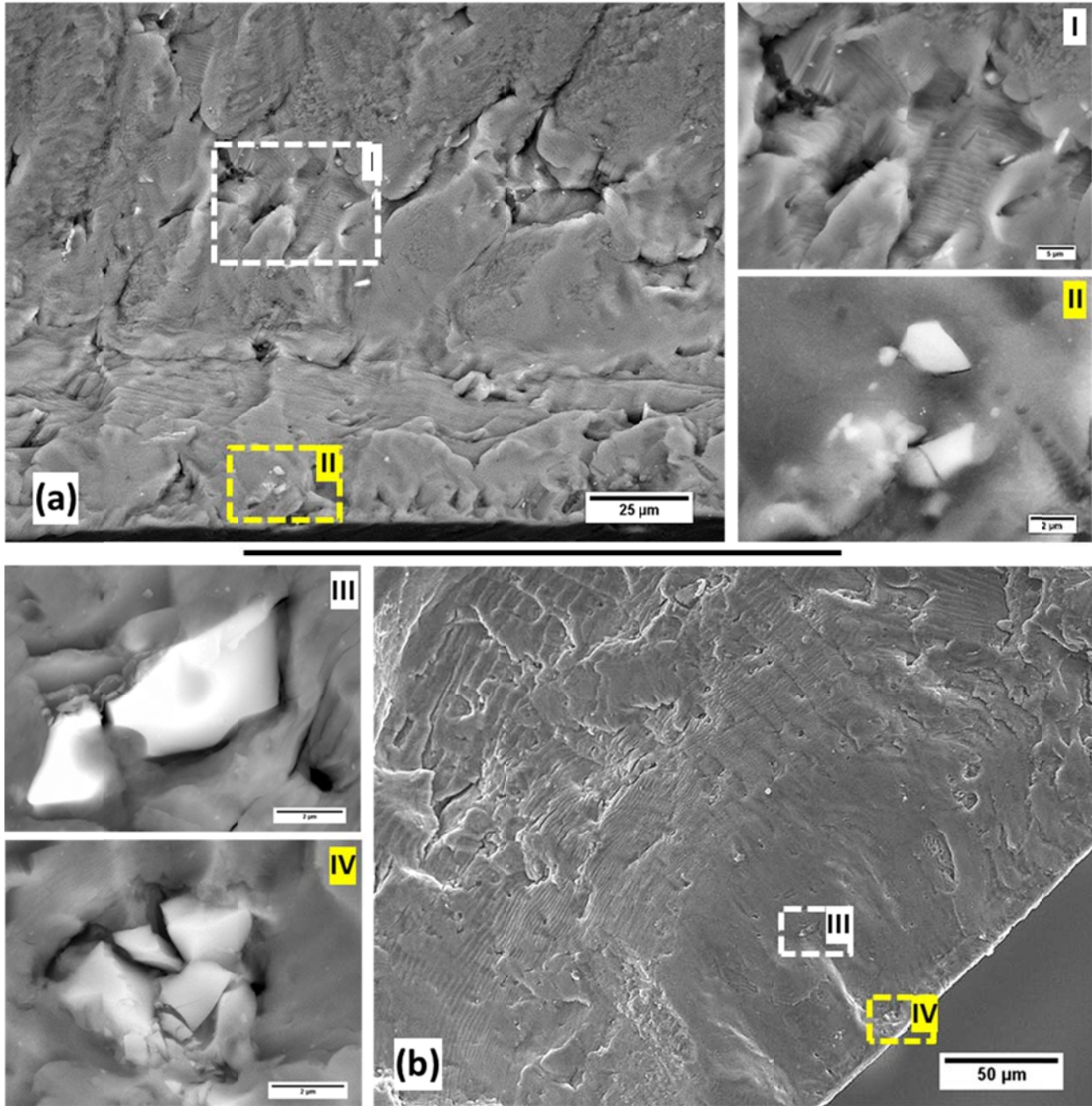


Figure 12. SEM fractography ($R=-1$) of as-received aa6061 a) 0.7% & b) 1.0% strain amplitude.

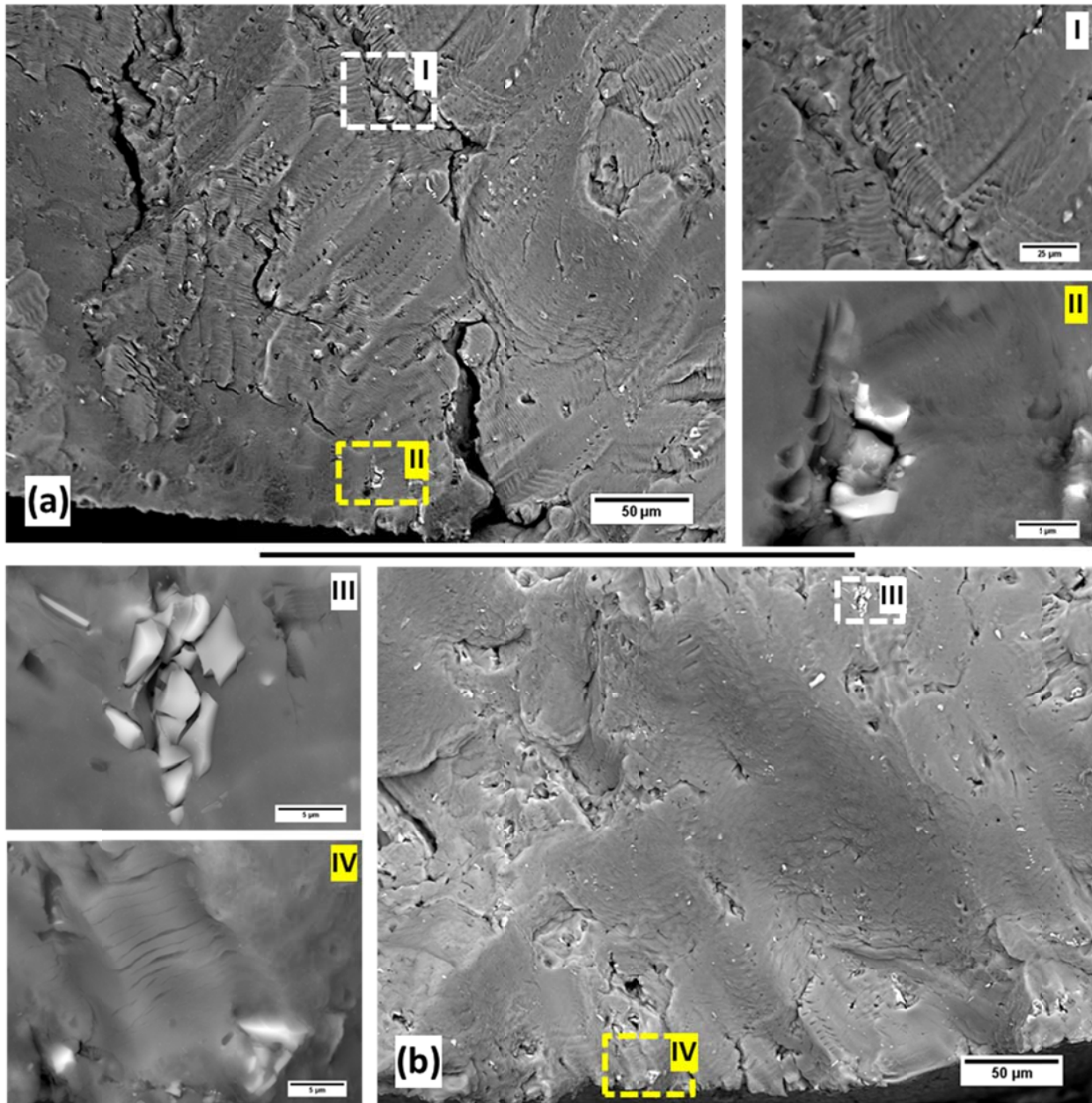


Figure 13. SEM fractography ($R=-1$) of annealed aa6061 a) 1.0% & b) 2.5% strain amplitude.

Micromechanics Simulations

In order to capture the behavior of AA6061 microstructure in the presence of uniaxial loads, an axisymmetric finite element model was implemented. For this model, a perfectly cylindrical, Fe-rich intermetallic precipitate (Young's Modulus of 134 MPa) representing a volume percentage of 2% versus the matrix material was used. The micromechanics-based simulation was conducted in Abaqus using an internal state variable (ISV) elastic-plastic constitutive material model using eight-node quadratic elements with an element density of 480 nodes along the particle circumference.

Delamination of the matrix/particle interface was assumed to be minimal and perfectly bonded. The particle was partitioned to replicate the load state of the material at particle fracture and just prior to crack propagation into the matrix. Figure 14a shows representation of the generated model with a fractured intermetallic located within cyclically loaded specimen. The generated localized strain field can be noted in figure 14b for a remote strain of 1.0%. The peak stress concentration generated by the particle fracture acts as the center-point for the plastic strain field propagation into the matrix.

From the finite elements results, the developed max root plastic shear strain at the stress intensifier can be captured as a power law function of the remote applied strain Figure 14c. Furthermore a correlation between the remote strain field and localized developed plasticity field can be derived, as shown in figure 14d. As such, the fatigue threshold damage limit and cyclic plastic strain percolation limits were determined. The fatigue damage threshold is the limit by which, when the applied localized strain is below this threshold, the resulting plasticity field is insufficient to produce a fatigue crack at the inclusion. The cyclic plastic strain percolation limit

represents the remote strain that produces fatigue crack growth unconstrained by the local notch root. These derived values are shown in Table 7.

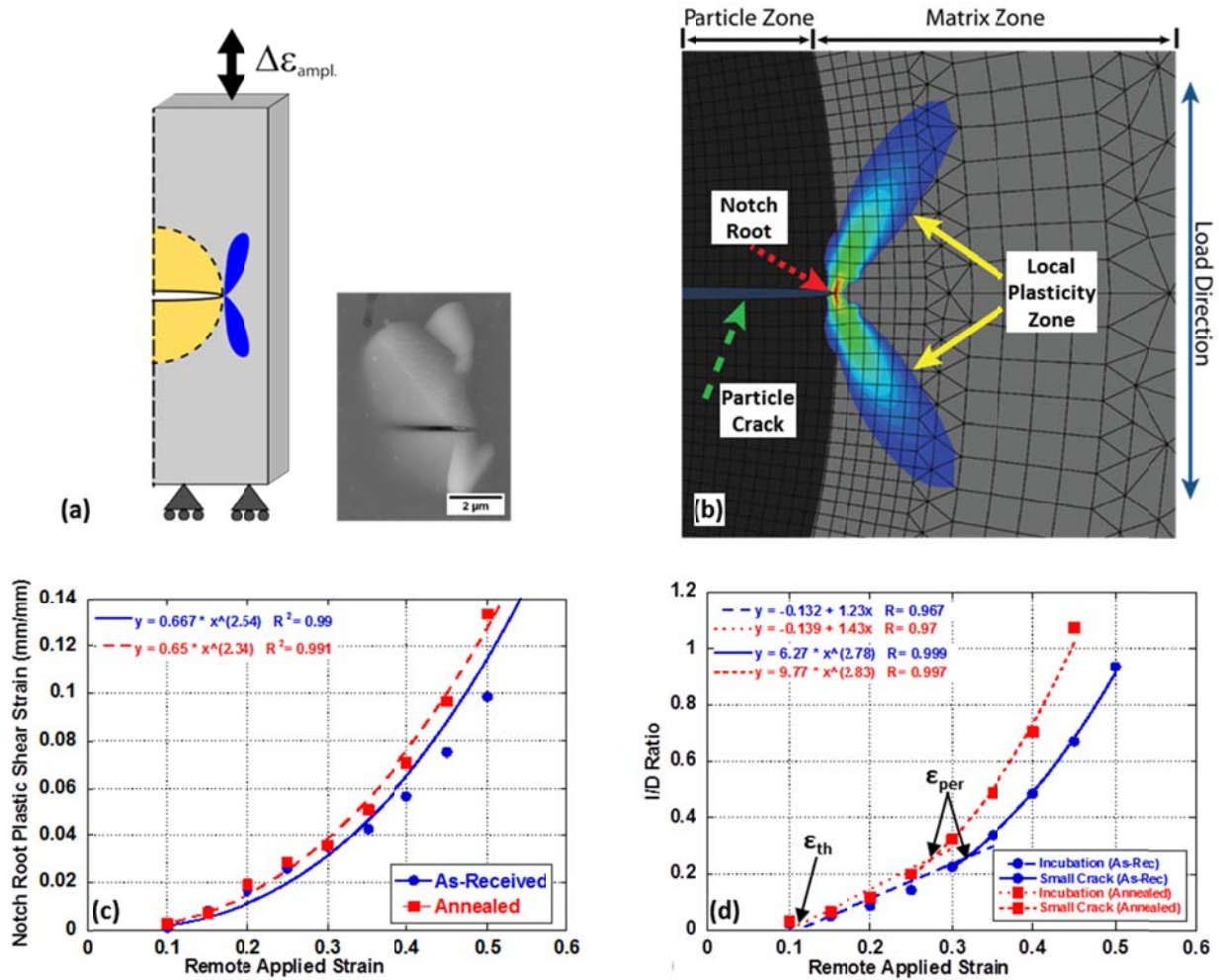


Figure 14. (a) FEA microstructure simulation illustration, (b) generated plasticity field contour map, (c) local plastic strain to remote strain plot & (d) l/d to remote strain plot.

Table 7. Microstructure-property MSF model coefficients

	Coefficients	As-Received	Annealed	Description
Crack Initiation	K'	392.9	390.2	Cyclic strength coefficient
	n'	0.0438	0.0761	Cyclic strain hardening coefficient
	C _{inc}	.64	.74	Constant related to C _m constant (CNC)
	C _m	0.623	0.6	Ductility coefficient in modified Coffin Manson Law
	A	-0.76	-0.76	Ductility exponent in modified Coffin Manson Law
	Q	1.2664	2.3313	Exponent in remote strain to local plastic shear strain
	y ₁	365.2	577.3	Constant in remote strain to local plastic shear strain
	y ₂	1422	1709	Linear constant in remote strain to local plastic shear strain
	ψ (psi)	1	1	Geometric factor in micromechanics study
	R	1	1	Exponent in micromechanics study
Small Crack (MSC/PSC)	E _{MODEX}	1	1	Shape parameter of Young's modulus
	PART _{EXP}	1	1	Shape parameter of particle size
	Ω	0.5	0.5	Omega
	A _i	0.25	0.25	Initial crack size contribution
	Θ	1.0	1.0	Load path dependent parameter
	Z	1.35	0.95	Exponent in small crack growth
	CI	16000	16000	HCF constant in small crack growth
	CII	0.07	0.07	LCF constant in small crack growth
	χ	0.425	0.325	Crack growth rate constant
	CTD _{TH}	0.000285	0.000285	CTD threshold value
A _{final}	450	450	Final crack size length (microns)	
DCS _{EXP}	1	1	Grain size constant (G)	
PORE _{EXP}	0	0	Effect of pore size to local plastic strain	
GO-EXP	0	0	Grain orientation constant	
E _{perc}	0.324%	0.278%	Percolation limit	
E _{th}	0.140%	0.126%	Plasticity threshold limit	
GS	12.3	14.8	Grain size (microns)	
G0	2.07	1.53	Grain orientation	

Fatigue Model Correlation

Fatigue crack growth rate results were collected through direct measurement of striations by means of scanning electron microscopy. Figure 15 shows that the propagation of the crack in both as-received and annealed conditions was very similar in most respects. The annealed AA6061 was observed to have higher propagation rates, which was attributed to a reduction in

pinning sites due to heat treatment. The crack growth component of the MSF model discussed previously showed that the slight difference in propagation rate between heat treatments could be captured by accounting for the variance in the cyclic hardening constant and exponent grain size. To account of variance of growth rate due to increasing strain amplitude, the model was able to capture this change by increasing the microstructure driven, crack growth rate constant (χ), as seen in Figures 15a & 15b.

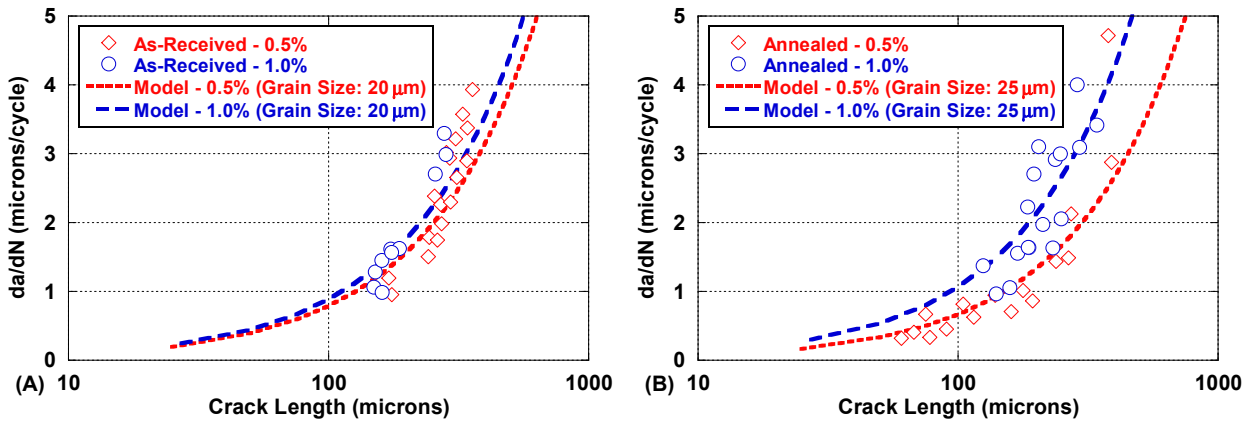


Figure 15. MSF crack growth model sensitivity charts a) as-received & b) annealed.

Figure 16 shows the comparison of the MSF model to the experimental strain life results of the 6061-T6 in the as-received, and annealed condition. The correlation process of the MSF model to the experimental data resulted in a unique set of parameters. While, the fit of the MSF model to the experimental results shown in Figure 11 is not a precise correlation, the model captured the overall behavior of the material in both conditions during fatigue loading. Table 7 provides a list of the modeling parameters used to achieve the fit in Figure 16. The incubation life of the material was captured directly in the derived mechanical data collected and the subsequent results from the micromechanical simulations. The contribution of small crack was developed using the experimentally derived values unique to each heat treatment state and universal fitting constants and exponents. Figure 17 shows the sensitivity of the MSF model to

particle size, a feature vital in capturing the fatigue behavior of the target material as crack initiation can be attributed to the initial failure of very large intermetallic particles within the matrix as stated earlier. From figure 17, it can be seen that the model can capture the variability of fatigue life of the material simply through varying the mean particle size by $\pm 1/2$ standard deviation.

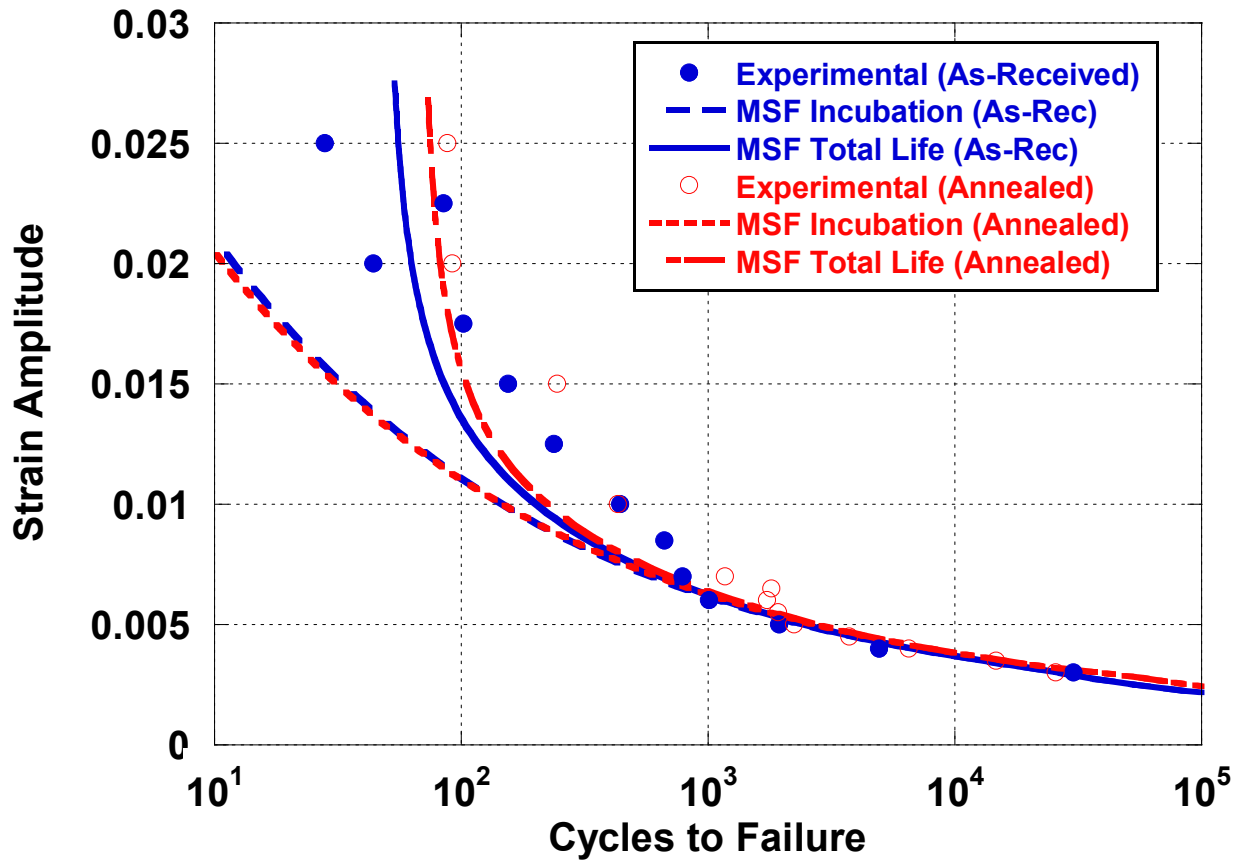


Figure 16. Fully reversing fatigue plot with MSF incubation and total strain-life results.

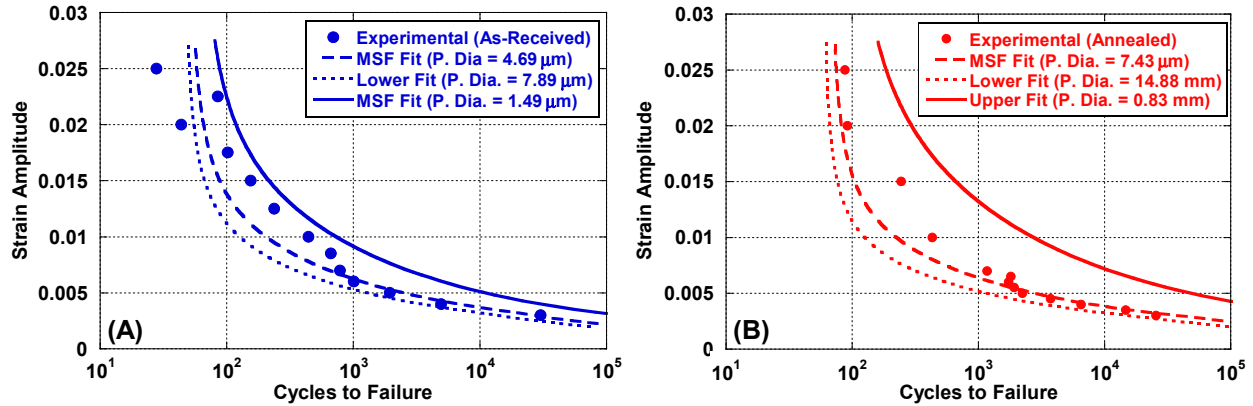


Figure 17. MSF fatigue fit plots for (a) as-received & (b) annealed states with upper and lower boundaries formed by $\pm \frac{1}{2}$ std. dev of the mean particle size.

The variance in fatigue life contribution as a percentage of total predicted fatigue life for AA6061 is shown in Figure 18. The correlation between incubation percentage contribution and remote applied strain amplitude has been well established as being inversely related (Y. Xue, El Kadiri, et al. 2007), as the progressive increase in applied load produces a convergence of the localized plastic strain field at inclusions within the material. This has been shown to act as an indicator of the onset of fatigue crack initiation at the root of a developing micro-notch near hard second phase inclusions (precipitates), as this behavior can accelerate the process of incubation as the local plastic shear strain field approaches saturation (unity) (Ken Gall et al. 2000). Therefore, as the material experiences higher strain amplitudes, the developed higher local shear strain at the microscopic notch will produce small crack growth earlier during load cycling leading to a dominant crack growth mechanism. Inversely, as the remote applied load decreases the dominant failure mechanism shifts to dominant incubation as the local shear strain at the micro-notch transitions from unconstrained to constrained microplasticity, increasing the contribution of incubation on the fatigue life of AA6061.

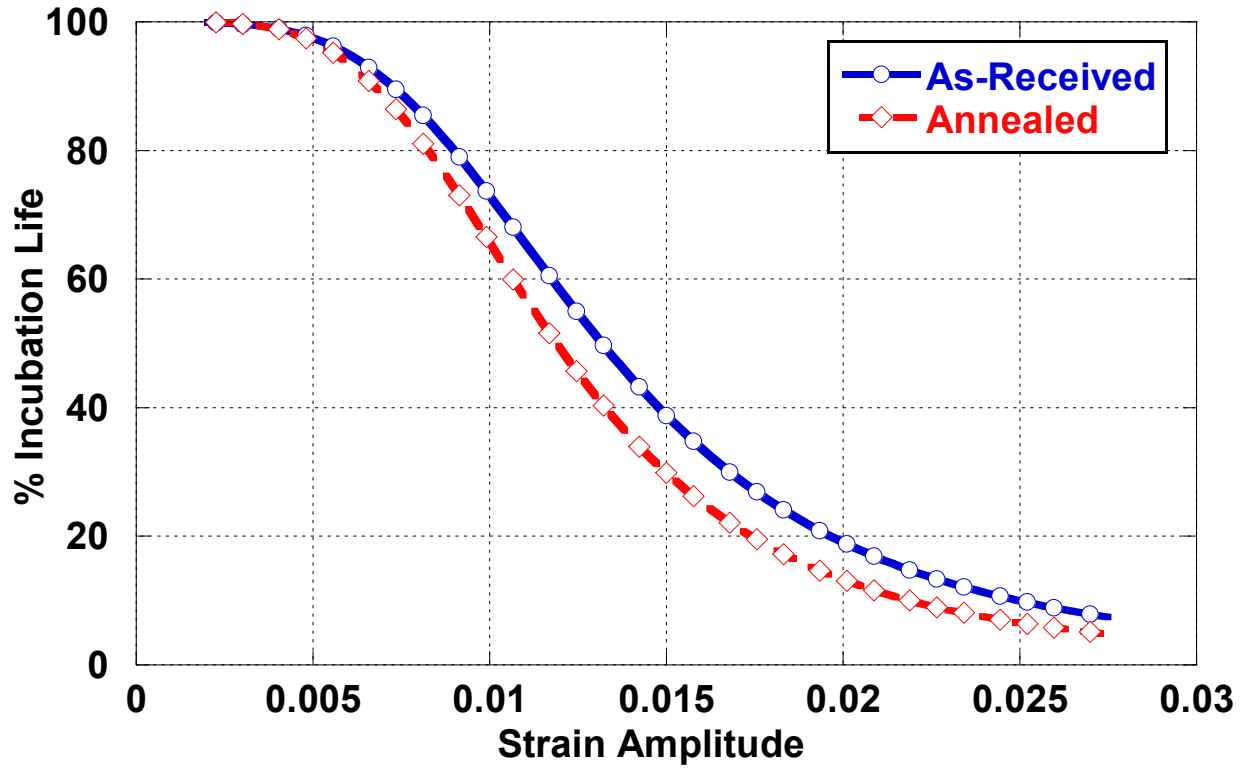


Figure 18. Predicted percentage contribution of incubation life to total fatigue life of as-received and annealed states.

CONCLUSIONS

The focus of this study was to quantify and capture the mechanical behavior in an extruded 6061 aluminum alloy. A series of experiments in quasi-static, tension-followed-by-compression and compression-followed-by-tension, and cycled to failure were performed. This study was able to establish several trends in the evolution of mechanical properties due to heat exposure in the form of single cycle partial annealing in ambient air environments. This study also showed that an internal state variable based plasticity model and microstructurally sensitive, multi-stage fatigue model can predict the strain-life of a set of materials with disparate thermal exposure histories by capturing the variance in damage developed within the matrix and distribution secondary phases. From analysis of both quasi-static and cyclic behavior of uniaxial loaded AA6061 in T6 and annealed conditions, the following conclusions were made:

- a) The development of the BE was observed in a dispersion hardened peak aged aluminum alloy (6061-T6), at the high reversed strain amplitudes applied. BE was seen to increase with increasing strain amplitudes in tension-followed-by-compression loadings and remain constant in compression-followed-by-tension loading.
- b) The effect of the annealing schedule at a temperature of 316°C led to an increase in the BE in the material and a low sensitivity to the applied strain amplitude.
- c) The material behavior seen in the experiments was effectively captured by the internal state variable plasticity and damage model. This was accomplished successfully through the use of both isotropic and kinematic hardening, void/crack-nucleation, growth, and

calescence variables. The ISV model demonstrated good correlation between the as-received and the annealed conditions by simply including the corresponding mechanical properties of the material; the evolution of plasticity due to moderate temperature exposure was captured.

- d) It is important to note that softening observed is attributed to the relaxation of internal stresses from the build-up of dislocations around these hard precipitates. As such, through the combination of kinematic and isotropic hardening, and comprehensive damage laws, the ISV model captured the BE for extruded AA6061.
- e) Strain-life fatigue results of the AA6061 material exhibited minimal scatter correlation with increasing fatigue life with decreasing strain amplitude. AA6061 cyclic behavior was dominated by strain softening to failure even in the presence of annealing. The material showed limited reaction to the introduction of positive load ratios in relation to its fatigue life.
- f) SEM Fractography showed the occurrence of closely packed clusters and/or fractured particles. Striations were observed within 500 nanometers of fractured particles in both treatment states.
- g) In spite of having dissimilar monotonic and cyclic mechanical properties, the AA6061 specimens did not exhibit widely varying crack propagation behavior due to annealing.
- h) Micromechanical simulations were run that were shown to be effective in capturing the effective of remote applied strain on the development of local remote shear strain at the root of the micro-notch developed at the hard precipitates distributed throughout AA6061. These simulations were shown to be effective in capturing the evolution of plastic field development with varying heat treatment states. With softening of the material

producing larger strain fields, which increases the influence of particle on incubation life and offsets the inverse effect of faster root-notch shear strain at the precipitate.

- i) The MSF model was shown to be effective in capturing the fatigue behavior of AA6061. The development of fatigue behavior seen too be dependent on the level of localized plastic deformation generated within the material during loading, higher strain amplitudes producing greater effect and accelerated crack propagation. The model was shown be effective in capturing the slight changes in fatigue life within the material due to varying heat treatments.

REFERENCES

- Abedrabbo, Nader, Farhang Pourboghrat, and John Carsley. 2006. "Forming of Aluminum Alloys at Elevated Temperatures – Part 1: Material Characterization." *International Journal of Plasticity* 22 (2) (February): 314–341. doi:10.1016/j.ijplas.2005.03.005. <http://linkinghub.elsevier.com/retrieve/pii/S0749641905000641>.
- Abel, A. 1987. "Historical Perspectives and Some of the Main Features of the Bauschinger Effect." *Materials Forum* 10 (1): 11–26. <http://cat.inist.fr/?aModele=afficheN&cpsidt=7385260>.
- Abel, A., and H. Muir. 1972. "The Bauschinger Effect and Discontinuous Yielding." *Philosophical Magazine* 26 (2) (August): 489–504. doi:10.1080/14786437208227444. <http://www.tandfonline.com/doi/abs/10.1080/14786437208227444>.
- Abood, Adnan N., Ali H. Saleh, and Zainab W. Abdullah. 2013. "Effect of Heat Treatment on Strain Life of Aluminum Alloy AA 6061." *Journal of Materials Science Research* 2 (2) (January 30): 51–59. doi:10.5539/jmsr.v2n2p51. <http://www.ccsenet.org/journal/index.php/jmsr/article/view/20691>.
- Agarwal, H, and A.M. Gokhale. 2003. "Void Growth in 6061-Aluminum Alloy under Triaxial Stress State." *Materials Science and ...* 341. <http://www.sciencedirect.com/science/article/pii/S0921509302000734>.
- Aizpuru, N., D. Le, J. McDonald, L. McLennan, S. Tewfik, E.W. Lee, D. Piatkowski, et al. 2005. "The Effect of Flash Annealing on the Mechanical and Electrical Properties of Previously Used AM2 Mats Composed of Al 6061-T6." *Engineering Failure Analysis* 12 (5) (October): 691–698. doi:10.1016/j.engfailanal.2004.12.001. <http://linkinghub.elsevier.com/retrieve/pii/S135063070500021X>.
- Allison, P. G., Y. Hammi, J. B. Jordon, and M. F. Horstemeyer. 2013. "Modelling and Experimental Study of Fatigue of Powder Metal Steel (FC-0205)." *Powder Metallurgy* 56 (5) (December): 388–396. doi:10.1179/1743290113Y.0000000063.
- Arsenault, R.J., and S.B. Wu. 1987. "The Strength Differential and Bauschinger Effects in SiC/Al Composites." *Materials Science and Engineering* 96 (null) (December): 77–88. doi:10.1016/0025-5416(87)90542-8. [http://dx.doi.org/10.1016/0025-5416\(87\)90542-8](http://dx.doi.org/10.1016/0025-5416(87)90542-8).

- Bammann, D.J., M.L. Chiesa, M.F. Horstemeyer, and L.I. Weingarten. 1993. "Failure of Ductile Materials Using Finite Element Methods." In *Structural Crashworthiness and Failure*, edited by Norman Jones and Tomasz Wierzbicki. London: Elsevier Applied Science.
- Bammann, DJ, and EC Aifantis. 1989. "A Damage Model for Ductile Metals." *Nuclear Engineering and Design* 116: 355–362.
<http://www.sciencedirect.com/science/article/pii/0029549389900952>.
- Bammann, Douglas J. 1990. "Modeling Temperature and Strain Rate Dependent Large Deformations of Metals." *Applied Mechanics Reviews* 43.
- Bate, PS, and DV Wilson. 1986. "Analysis of the Bauschinger Effect." *Acta Metallurgica* 34 (6).
<http://www.sciencedirect.com/science/article/pii/0001616086902208>.
- Bonollo, F, L Ceschini, and GL Garagnani. 1997. "Mechanical and Impact Behaviour of (Al₂O₃)p/2014 and (Al₂O₃)p/6061 Al Metal Matrix Composites in the 25–200° C Range." *Applied Composite Materials* 4: 173–185.
<http://www.springerlink.com/index/v020t083280454g4.pdf>.
- Brammer, A. T., J. B. Jordon, P. G. Allison, and M. E. Barkey. 2012. "Strain-Controlled Low-Cycle Fatigue Properties of Extruded 6061-T6 Aluminum Alloy." *Journal of Materials Engineering and Performance* (October 9): 3–5. doi:10.1007/s11665-012-0411-0.
<http://www.springerlink.com/index/10.1007/s11665-012-0411-0>.
- Brown, Donald W., A. Jain, Sean R. Agnew, and Bjørn Clausen. 2007. "Twinning and Detwinning during Cyclic Deformation of Mg Alloy AZ31B." *Materials Science Forum* 539-543: 3407–3413. doi:10.4028/www.scientific.net/MSF.539-543.3407.
<http://www.scientific.net/MSF.539-543.3407>.
- Buckley, S.N., and K.M. Entwistle. 1956. "The Bauschinger Effect in Super-Pure Aluminum Single Crystals and Polycrystals." *Acta Metallurgica* 4 (4) (July): 352–361.
 doi:10.1016/0001-6160(56)90023-2. [http://dx.doi.org/10.1016/0001-6160\(56\)90023-2](http://dx.doi.org/10.1016/0001-6160(56)90023-2).
- Caceres, CH, JR Griffiths, and P Reiner. 1996. "The Influence of Microstructure on the Bauschinger Effect in an Al-Si-Mg Casting Alloy." *Acta Materialia* 7151 (95): 15–23.
<http://www.sciencedirect.com/science/article/pii/1359645495001716>.
- Caton, M.J, J.W Jones, and J.E Allison. 2001. "The Influence of Heat Treatment and Solidification Time on the Behavior of Small-Fatigue-Cracks in a Cast Aluminum Alloy." *Materials Science and Engineering: A* 314 (1-2) (September): 81–85. doi:10.1016/S0921-5093(00)01916-X. <http://linkinghub.elsevier.com/retrieve/pii/S092150930001916X>.
- Chan, Kwai S. 2010. "Roles of Microstructure in Fatigue Crack Initiation." *International Journal of Fatigue* 32 (9) (September): 1428–1447. doi:10.1016/j.ijfatigue.2009.10.005.
<http://www.sciencedirect.com/science/article/pii/S0142112309002989>.

- Chen, Z, and K Tokaji. 2004. "Effects of Particle Size on Fatigue Crack Initiation and Small Crack Growth in SiC Particulate-Reinforced Aluminium Alloy Composites." *Materials Letters* 58 (17-18) (July): 2314–2321. doi:10.1016/j.matlet.2004.02.034. <http://linkinghub.elsevier.com/retrieve/pii/S0167577X04001533>.
- Choi, SH, F Barlat, and J Liu. 2001. "Effect of Precipitates on Plastic Anisotropy for Polycrystalline Aluminum Alloys." *Metallurgical and Materials Transactions A* 32 (September): 2239–2247. <http://link.springer.com/article/10.1007/s11661-001-0199-2>.
- Chun, B.K., J.T. Jinn, and J.K. Lee. 2002. "Modeling the Bauschinger Effect for Sheet Metals, Part I: Theory." *International Journal of Plasticity* 18 (5-6) (October): 571–595. doi:10.1016/S0749-6419(01)00046-8. <http://linkinghub.elsevier.com/retrieve/pii/S0749641901000468>.
- Corbin, S.F., D.S. Wilkinson, and J.D. Embury. 1996. "The Bauschinger Effect in a Particulate Reinforced Al Alloy." *Materials Science and Engineering: A* 207 (1) (March): 1–11. doi:10.1016/0921-5093(95)10028-8. <http://linkinghub.elsevier.com/retrieve/pii/0921509395100288>.
- Eggertsen, P.-a., and K. Mattiasson. 2009. "On the Modelling of the Bending–unbending Behaviour for Accurate Springback Predictions." *International Journal of Mechanical Sciences* 51 (7) (July): 547–563. doi:10.1016/j.ijmecsci.2009.05.007. <http://linkinghub.elsevier.com/retrieve/pii/S0020740309001040>.
- Embury, J.D. 1987. "Structural Aspects of the Bauschinger Effect." *Materials Forum* 10: 27–32.
- Gall, K, Nancy Yang, and Mark Horstemeyer. 1999. "The Debonding and Fracture of Si Particles during the Fatigue of a Cast Al-Si Alloy." ... *Materials Transactions A* 30 (December): 3079–3088. <http://link.springer.com/article/10.1007/s11661-999-0218-2>.
- Gall, Ken, Mark Horstemeyer, David L. McDowell, and Jinghong Fan. 2000. "Finite Element Analysis of the Stress Distributions near Damaged Si Particle Clusters in Cast Al-Si Alloys." *Mechanics of Materials* 32 (5) (May): 277–301. doi:10.1016/S0167-6636(00)00003-X. <http://linkinghub.elsevier.com/retrieve/pii/S016766360000003X>.
- Gan, W, Peihui Zhang, RH Wagoner, and GS Daehn. 2006. "Effect of Load Redistribution in Transient Plastic Flow." *Metallurgical and Materials ...* 37 (July). <http://link.springer.com/article/10.1007/BF02586130>.
- Gould, D., P. B. Hirsch, and F. J. Humphreys. 1974. "The Bauschinger Effect, Work-Hardening and Recovery in Dispersion-Hardened Copper Crystals." *Philosophical Magazine* 30 (6) (December): 1353–1377. doi:10.1080/14786437408207287. <http://dx.doi.org/10.1080/14786437408207287>.
- Gracio, J.J., F. Barlat, E.F. Rauch, P.T. Jones, V.F. Neto, and a.B. Lopes. 2004. "Artificial Aging and Shear Deformation Behaviour of 6022 Aluminium Alloy." *International Journal of*

Plasticity 20 (3) (March): 427–445. doi:10.1016/S0749-6419(03)00095-0.
<http://linkinghub.elsevier.com/retrieve/pii/S0749641903000950>.

Guo, Y.B., Q. Wen, and M.F. Horstemeyer. 2005. “An Internal State Variable Plasticity-Based Approach to Determine Dynamic Loading History Effects on Material Property in Manufacturing Processes.” *International Journal of Mechanical Sciences* 47 (9) (September): 1423–1441. doi:10.1016/j.ijmecsci.2005.04.015.
<http://linkinghub.elsevier.com/retrieve/pii/S0020740305001347>.

Hayhurst, D. R., F. A. Leckie, and McDow. 1985. “Damage Growth under Nonproportional Loading.” In *Multiaxial Fatigue - STP853*, 553–558.

Hidayetoglu, Tulin K., Paul N. Pica, and W.L. Haworth. 1985. “Aging Dependence of the Bauschinger Effect in Aluminum Alloy 2024.” *Materials Science and Engineering* 73 (null) (August): 65–76. doi:10.1016/0025-5416(85)90296-4. [http://dx.doi.org/10.1016/0025-5416\(85\)90296-4](http://dx.doi.org/10.1016/0025-5416(85)90296-4).

Horstemeyer, M F. 2001. “A New Design Paradigm Using Part 1 : Monotonic Loading Conditions” (March).

———. 2010. “Chapter 4 - Multiscale Modeling: A Review.” In *Practical Aspects of Computational Chemistry*, edited by Jerzy Leszczynski and Manoj K. Shukla, 87–135. Dordrecht: Springer Netherlands. doi:10.1007/978-90-481-2687-3.
<http://www.springerlink.com/index/10.1007/978-90-481-2687-3>.

Horstemeyer, M. F., and S. Ramaswamy. 2000. “On Factors Affecting Localization and Void Growth in Ductile Metals: A Parametric Study.” *International Journal of Damage Mechanics* 9 (1) (January 1): 5–28. doi:10.1177/105678950000900102.
<http://ijd.sagepub.com/cgi/doi/10.1177/105678950000900102>.

Horstemeyer, M.F., J. Lathrop, A.M. Gokhale, and M. Dighe. 2000. “Modeling Stress State Dependent Damage Evolution in a Cast Al–Si–Mg Aluminum Alloy.” *Theoretical and Applied Fracture Mechanics* 33 (1) (February): 31–47. doi:10.1016/S0167-8442(99)00049-X. [http://dx.doi.org/10.1016/S0167-8442\(99\)00049-X](http://dx.doi.org/10.1016/S0167-8442(99)00049-X).

Horstemeyer, Mark F. 1998. “Damage Influence on Bauschinger Effect of a Cast A356 Aluminum Alloy.” *Scripta Materialia* 39 (11) (November): 1491–1495. doi:10.1016/S1359-6462(98)00343-1.
<http://linkinghub.elsevier.com/retrieve/pii/S1359646298003431>.

Horstemeyer, MF, and AM Gokhale. 1999. “A Void–crack Nucleation Model for Ductile Metals.” *International Journal of Solids and ...*: 4918–4944.
<http://www.sciencedirect.com/science/article/pii/S002076839800239X>.

- Jordon, J B, J B Gibson, and M F Horstemeyer. 2011. "Experiments and Modeling of Fatigue of an Extruded Mg AZ61 Alloy." In *Magnesium Technology 2011*, 55–60. John Wiley & Sons, Inc. doi:10.1002/9781118062029.ch13.
- Jordon, J. B., and M. F. Horstemeyer. 2014. "Microstructure-Sensitive Fatigue Modeling of AISI 4140 Steel." *Journal of Engineering Materials and Technology* 136 (2) (February 5): 021004. doi:10.1115/1.4025424.
<http://materialstechnology.asmedigitalcollection.asme.org/article.aspx?doi=10.1115/1.4025424>.
- Jordon, J.B., J.B. Gibson, M.F. Horstemeyer, H. El Kadiri, J.C. Baird, and A.a. Luo. 2011. "Effect of Twinning, Slip, and Inclusions on the Fatigue Anisotropy of Extrusion-Textured AZ61 Magnesium Alloy." *Materials Science and Engineering: A* 528 (22-23) (August): 6860–6871. doi:10.1016/j.msea.2011.05.047.
<http://linkinghub.elsevier.com/retrieve/pii/S092150931100596X>.
- Jordon, J.B., M.F. Horstemeyer, K. Solanki, and Y. Xue. 2007. "Damage and Stress State Influence on the Bauschinger Effect in Aluminum Alloys." *Mechanics of Materials* 39 (10) (October): 920–931. doi:10.1016/j.mechmat.2007.03.004.
<http://linkinghub.elsevier.com/retrieve/pii/S0167663607000579>.
- Jordon, J.B., M.F. Horstemeyer, N. Yang, J.F. Major, K.a. Gall, J. Fan, and D.L. McDowell. 2009. "Microstructural Inclusion Influence on Fatigue of a Cast A356 Aluminum Alloy." *Metallurgical and Materials Transactions A* 41 (2) (November 4): 356–363. doi:10.1007/s11661-009-0088-7. <http://www.springerlink.com/index/10.1007/s11661-009-0088-7>.
- Kadiri, Haitham El, Ybin Xue, M.F. Horstemeyer, J. Brian Jordon, and Paul T. Wang. 2006. "Identification and Modeling of Fatigue Crack Growth Mechanisms in a Die-Cast AM50 Magnesium Alloy." *Acta Materialia* 54 (19) (November): 5061–5076. doi:10.1016/j.actamat.2006.06.039.
<http://linkinghub.elsevier.com/retrieve/pii/S1359645406004599>.
- Kassner, M.E., P Geantil, LE Levine, and BC Larson. 2008. "Backstress, The Bauschinger Effect, and Cyclic Deformation." *Materials Science Forum* 605: 39–51. http://www.osti.gov/energycitations/product.biblio.jsp?osti_id=946494.
- Kishi, T, and T Tanabe. 1973. "The Bauschinger Effect and Its Role in Mechanical Anisotropy." *Journal of the Mechanics and Physics of Solids* 21: 303–315. <http://www.sciencedirect.com/science/article/pii/0022509673900021>.
- Kliauga, A. M., and M. Ferrante. 2005. "Liquid Formation and Microstructural Evolution during Re-Heating and Partial Melting of an Extruded A356 Aluminium Alloy." *Acta Materialia* 53 (2) (January): 345–356. doi:10.1016/j.actamat.2004.09.030. <http://linkinghub.elsevier.com/retrieve/pii/S1359645404005725>.

- Kumai, S, JE King, and JF Knott. 1990. "Short and Long Fatigue Crack Growth in a SiC Reinforced Aluminium Alloy." *Fatigue & Fracture of Engineering Materials & Structures* 13 (5): 511–524. <http://onlinelibrary.wiley.com/doi/10.1111/j.1460-2695.1990.tb00621.x/abstract>.
- Lassance, D, D Fabregue, F Delannay, and T Pardoën. 2007. "Micromechanics of Room and High Temperature Fracture in 6xxx Al Alloys." *Progress in Materials Science* 52 (1) (January): 62–129. doi:10.1016/j.pmatsci.2006.06.001. <http://linkinghub.elsevier.com/retrieve/pii/S0079642506000399>.
- Levin, M, and B Karlsson. 1993. "Crack Initiation and Growth during Low-Cycle Fatigue of Discontinuously Reinforced Metal-Matrix Composites." *International Journal of Fatigue* 15 (5) (September): 377–387. doi:10.1016/0142-1123(93)90483-7. <http://linkinghub.elsevier.com/retrieve/pii/0142112393904837>.
- Liangsén, Chen, and Z Xinghua. 1999. "A Mathematical Theory of Materials with Elastic Range and the Definition of Back Stress Tensor." *Applied Mathematics and Mechanics* 20 (5): 476–484. <http://link.springer.com/article/10.1007/BF02463743>.
- Liao, S.H., P.W. Kao, and C.P. Chang. 1997. "The Bauschinger Effect in Fine-Grained Al-Ti Alloys Prepared by Mechanical Alloying." *Scripta Materialia* 36 (11) (June): 1227–1232. doi:10.1016/S1359-6462(97)00022-5. <http://linkinghub.elsevier.com/retrieve/pii/S1359646297000225>.
- Lipkin, J, JC Swearingen, and CH Karnes. 1973. "Mechanical Properties of 6061 Al-Mg-Si Alloy after Very Rapid Heating." ... *of the Mechanics and Physics of ...* 21. <http://www.sciencedirect.com/science/article/pii/002250967390032X>.
- Lloyd, DJ. 1977. "The Bauschinger Effect in Polycrystalline Aluminium Containing Coarse Particles." *Acta Metallurgica* (A ci). <http://www.sciencedirect.com/science/article/pii/000161607790236X>.
- Lugo, M., J.B. Jordon, K.N. Solanki, L.G. Hector, J.D. Bernard, a.a. Luo, and M.F. Horstemeyer. 2013. "Role of Different Material Processing Methods on the Fatigue Behavior of an AZ31 Magnesium Alloy." *International Journal of Fatigue* 52 (July): 131–143. doi:10.1016/j.ijfatigue.2013.02.017.
- Lugo, Marcos, Jason E. Fountain, Justin M. Hughes, Jean-Luc Bouvard, and Mark F. Horstemeyer. 2014. "Microstructure-Based Fatigue Modeling of an Acrylonitrile Butadiene Styrene (ABS) Copolymer." *Journal of Applied Polymer Science* 131 (20) (October 15): n/a–n/a. doi:10.1002/app.40882. <http://doi.wiley.com/10.1002/app.40882>.
- Margolin, H, F Hazaveh, and H Yaguchi. 1978. "The Grain Boundary Contribution to the Bauschinger Effect." *Scripta Metallurgica* 12: 1141–1145. <http://scholar.google.com/scholar?hl=en&btnG=Search&q=intitle:The+Grain+Boundary+Contribution+to+the+Bauschinger+Effect#0>.

- McCullough, R. R., J. B. Jordon, A. T. Brammer, K. Manigandan, T. S. Srivatsan, P. G. Allison, and T. W. Rushing. 2013. "A Fatigue Model for Discontinuous Particulate-Reinforced Aluminum Alloy Composite: Influence of Microstructure." *Journal of Materials Engineering and Performance* 23 (1) (November 19): 65–76. doi:10.1007/s11665-013-0766-x. <http://link.springer.com/10.1007/s11665-013-0766-x>.
- McDowell, D.L., K. Gall, M.F. Horstemeyer, and J. Fan. 2003. "Microstructure-Based Fatigue Modeling of Cast A356-T6 Alloy." *Engineering Fracture Mechanics* 70 (1) (January): 49–80. doi:10.1016/S0013-7944(02)00021-8. <http://linkinghub.elsevier.com/retrieve/pii/S0013794402000218>.
- McDowell, DL. 1997a. "An Engineering Model for Propagation of Small Cracks in Fatigue." *Engineering Fracture Mechanics* 56 (3): 357–377. <http://www.sciencedirect.com/science/article/pii/S0013794496000574>.
- . 1997b. "Multiaxial Small Fatigue Crack Growth in Metals." *International Journal of Fatigue* 19 (1): 127–135. <http://www.sciencedirect.com/science/article/pii/S0142112397000145>.
- Miller, M. 1999. "Reverse Yield Experiments and Internal Variable Evolution in Polycrystalline Metals." *International Journal of Plasticity* 15 (1) (March): 93–117. doi:10.1016/S0749-6419(98)00046-1. [http://dx.doi.org/10.1016/S0749-6419\(98\)00046-1](http://dx.doi.org/10.1016/S0749-6419(98)00046-1).
- Miller, W.S, L. Zhuang, J. Bottema, A.J. Wittebrood, P. De Smet, A. Haszler, and A. Vieregge. 2000. "Recent Development in Aluminium Alloys for the Automotive Industry." *Materials Science and Engineering: A* 280 (1): 37–49. <http://www.sciencedirect.com/science/article/pii/S092150939900653X>.
- Minakawa, K., G. Levan, and A. J. McEvily. 1986. "The Influence of Load Ratio on Fatigue Crack Growth in 7090-t6 and in 9021-t4 P/m Aluminum Alloys." *Metallurgical and Materials Transactions A* 17 (10) (October): 1787–1795. doi:10.1007/BF02817276. <http://link.springer.com/10.1007/BF02817276>.
- Mohammadtaheri, M. 2012. "A New Metallographic Technique for Revealing Grain Boundaries in Aluminum Alloys." *Metallography, Microstructure, and Analysis* 1 (5) (October 6): 224–226. doi:10.1007/s13632-012-0033-9. http://download.springer.com/static/pdf/201/art:10.1007/s13632-012-0033-9.pdf?auth66=1396925793_029b299443d42670b2cfc61646c2139c&ext=.pdf.
- Mrówka-Nowotnik, G. 2010. "Influence of Chemical Composition Variation and Heat Treatment on Microstructure and Mechanical Properties of 6xxx Alloys." *Archives of Materials Science and ...* 46 (2): 6–13. http://157.158.19.176/vol46_2/4623.pdf.
- Myhr, O.R., Ø. Grong, H.G. Fjær, and C.D. Marioara. 2004. "Modelling of the Microstructure and Strength Evolution in Al–Mg–Si Alloys during Multistage Thermal Processing." *Acta*

- Materialia* 52 (17) (October): 4997–5008. doi:10.1016/j.actamat.2004.07.002.
<http://linkinghub.elsevier.com/retrieve/pii/S135964540400401X>.
- Myriounis, D P, S T Hasan, and T E Matikas. 2008. “Microdeformation Behaviour of Al–SiC Metal Matrix Composites.” *Composite Interfaces* 15 (5): 495–514.
- Newman, J.C. 1995. “Fatigue-Life Prediction Methodology Using a Crack-Closure Model.” *Journal of Engineering Materials and Technology* 117 (4): 433–439.
- Ozturk, F., A. Sisman, S. Toros, S. Kilic, and R.C. Picu. 2010. “Influence of Aging Treatment on Mechanical Properties of 6061 Aluminum Alloy.” *Materials & Design* 31 (2) (February): 972–975. doi:10.1016/j.matdes.2009.08.017.
<http://dx.doi.org/10.1016/j.matdes.2009.08.017>.
- Pedersen, K.O., O.-G. Lademo, T. Berstad, T. Furu, and O.S. Hopperstad. 2008. “Influence of Texture and Grain Structure on Strain Localisation and Formability for AlMgSi Alloys.” *Journal of Materials Processing Technology* 200 (1-3) (May): 77–93.
doi:10.1016/j.jmatprotec.2007.08.040.
<http://www.sciencedirect.com/science/article/pii/S0924013607007790>.
- Pedersen, O.B., L.M. Brown, and W.M. Stobbs. 1981. “The Bauschinger Effect.” *Acta Metallurgica* 29: 1843–1850.
<http://scholar.google.com/scholar?hl=en&btnG=Search&q=intitle:THE+BAUSCHINGER+EFFECT#0>.
- Prietto, M., M. Tsang, S. Hernandez, J. Roepke, D. Piatkowski, E. Lee, P. Stoyanov, J. Ogren, and O.S. Es-Said. 2011. “The Effects of Heat Damage of Aluminum 6061-T6 AM2 Mats and High Power Run-Up Anchor.” *Engineering Failure Analysis* 18 (1) (January): 124–137.
doi:10.1016/j.engfailanal.2010.08.014.
<http://linkinghub.elsevier.com/retrieve/pii/S1350630710001445>.
- Proudhon, H., W.J. Poole, X. Wang, and Y. Bréchet. 2008. “The Role of Internal Stresses on the Plastic Deformation of the Al–Mg–Si–Cu Alloy AA6111.” *Philosophical Magazine* 88 (5) (February 11): 621–640. doi:10.1080/14786430801894569.
<http://www.tandfonline.com/doi/abs/10.1080/14786430801894569>.
- Rajagopalan, Jagannathan, Christian Rentenberger, H. Peter Karnthaler, Gerhard Dehm, and M. Taher a. Saif. 2010. “In Situ TEM Study of Microplasticity and Bauschinger Effect in Nanocrystalline Metals.” *Acta Materialia* 58 (14) (August): 4772–4782.
doi:10.1016/j.actamat.2010.05.013.
<http://linkinghub.elsevier.com/retrieve/pii/S1359645410002880>.
- Rauch, E.F., J.J. Gracio, F. Barlat, A.B. Lopes, and J. Ferreira Duarte. 2002. “Hardening Behavior and Structural Evolution upon Strain Reversal of Aluminum Alloys.” *Scripta Materialia* 46 (12) (June): 881–886. doi:10.1016/S1359-6462(02)00073-8.
<http://linkinghub.elsevier.com/retrieve/pii/S1359646202000738>.

- Rettberg, Luke H., J. Brian Jordon, Mark F. Horstemeyer, and J. Wayne Jones. 2012. "Low-Cycle Fatigue Behavior of Die-Cast Mg Alloys AZ91 and AM60." *Metallurgical and Materials Transactions A* 43 (7) (March 22): 2260–2274. doi:10.1007/s11661-012-1114-8. <http://www.springerlink.com/index/10.1007/s11661-012-1114-8>.
- Reynolds, A. P., and J. S. Lyons. 1997. "Isotropic and Kinematic Hardening in a Dispersion-Strengthened Aluminum Alloy." *Metallurgical and Materials Transactions A* 28 (5) (May): 1205–1211. doi:10.1007/s11661-997-0285-1. <http://link.springer.com/10.1007/s11661-997-0285-1>.
- Richeton, T., S. Berbenni, and M. Berveiller. 2009. "Grain-Size Dependent Accommodation due to Intragranular Distributions of Dislocation Loops." *Acta Materialia* 57 (5) (March): 1347–1356. doi:10.1016/j.actamat.2008.11.024. <http://linkinghub.elsevier.com/retrieve/pii/S1359645408008240>.
- Russell, A. M., and K. L. Lee. 2005. *Structure-Property Relations in Non-Ferrous Metals*. Wiley Interscience. New York: Wiley Interscience.
- Schikorra, M., L. Donati, L. Tomesani, and a. E. Tekkaya. 2007. "Microstructure Analysis of Aluminum Extrusion: Grain Size Distribution in AA6060, AA6082 and AA7075 Alloys." *Journal of Mechanical Science and Technology* 21 (10) (October): 1445–1451. doi:10.1007/BF03177357. <http://link.springer.com/10.1007/BF03177357>.
- Shin, C.S., and J.C. Huang. 2010. "Effect of Temper, Specimen Orientation and Test Temperature on the Tensile and Fatigue Properties of SiC Particles Reinforced PM 6061 Al Alloy." *International Journal of Fatigue* 32 (10) (October): 1573–1581. doi:10.1016/j.ijfatigue.2010.02.015. <http://dx.doi.org/10.1016/j.ijfatigue.2010.02.015>.
- Srivatsan, T. S., M Al-Hajri, B Hotton, and PC Lam. 2002. "Effect of Particulate Silicon Carbide on Cyclic Plastic Strain Response and Fracture Behavior of 6061 Aluminum Alloy Metal Matrix Composites." *Applied Composite Materials* 9: 131–153. <http://www.springerlink.com/index/edt87q1g0nharleu.pdf>.
- Srivatsan, T.S., S. Sriram, and C. Daniels. 1997. "Influence of Temperature on Cyclic Stress Response and Fracture Behavior of Aluminum Alloy 6061." *Engineering Fracture Mechanics* 56 (4): 531–550. <http://www.sciencedirect.com/science/article/pii/S0013794496001026>.
- Srivatsan, T.S., Koji Yamaguchi, and E.A. Starke. 1986. "The Effect of Environment and Temperature on the Low Cycle Fatigue Behavior of Aluminum Alloy 2020." *Materials Science and Engineering* 83 (1): 87–107. <http://www.sciencedirect.com/science/article/pii/002554168690176X>.
- Suresh, S. 1983. "Micromechanisms of Fatigue Crack Growth Retardation Following Overloads." *Engineering Fracture Mechanics* 18 (3): 577–593.

- Tamura, Shohei, Satoshi Sumikawa, Takeshi Uemori, Hiroshi Hamasaki, and Fusahito Yoshida. 2011. "Experimental Observation of Elasto-Plasticity Behavior of Type 5000 and 6000 Aluminum Alloy Sheets." *MATERIALS TRANSACTIONS* 52 (5): 868–875. doi:10.2320/matertrans.L-MZ201101. <http://joi.jlc.jst.go.jp/JST.JSTAGE/matertrans/L-MZ201101?from=CrossRef>.
- Tang, Tian, Youssef Hammi, M.F. Horstemeyer, and Paul Wang. 2012. "Finite Element Micromechanical Analysis of the Deformation and Stress State Dependent Damage Evolution in Fiber Reinforced Metal Matrix Composites." *Computational Materials Science* 59: 165–173. <http://www.sciencedirect.com/science/article/pii/S0927025612001383>.
- Taya, M., K.E. Lulay, K. Wakashima, and D.J. Lloyd. 1990. "Bauschinger Effect in Particulate SiC-6061 Aluminum Composites." *Materials Science and Engineering: A* 124 (2) (April): 103–111. doi:10.1016/0921-5093(90)90140-X. <http://linkinghub.elsevier.com/retrieve/pii/092150939090140X>.
- Tucker, M.T., M.F. Horstemeyer, W.R. Whittington, K.N. Solanki, and P.M. Gullett. 2010. "The Effect of Varying Strain Rates and Stress States on the Plasticity, Damage, and Fracture of Aluminum Alloys." *Mechanics of Materials* 42 (10) (October): 895–907. doi:10.1016/j.mechmat.2010.07.003. <http://linkinghub.elsevier.com/retrieve/pii/S0167663610000931>.
- Wang, L, ZM Sun, T Kobayashi, H Toda, and Z Wang. 1996. "Cyclic Deformation and Low Cycle Fatigue Behavior in a 6061Al/22vol% SiC Whisker Composite." *Materials Transactions, ...* 37 (4): 762–768. <http://www.jim.or.jp/journal/e/pdf3/37/04/762.pdf>.
- Wang, Q, N Kawagoishi, and Q Chen. 2006. "Fatigue and Fracture Behaviour of Structural Al-Alloys up to Very Long Life Regimes." *International Journal of Fatigue* 28 (11) (November): 1572–1576. doi:10.1016/j.ijfatigue.2005.09.017. <http://linkinghub.elsevier.com/retrieve/pii/S0142112306000934>.
- Wang, QG. 2004. "Plastic Deformation Behavior of Aluminum Casting Alloys A356/357." *Metallurgical and Materials Transactions A* 35 (September): 2707–2718. <http://link.springer.com/article/10.1007/s11661-004-0216-3>.
- Wilhelm, C., G. LaCaille, N. Wright, N. Ward, C. Shu, R. Painter, C. Vinquist, et al. 2009. "Mechanical Properties and Microstructure Characterization of Coated AM2 Al 6061-T6 Mats Exposed to Simulated Thermal Blast." *Engineering Failure Analysis* 16 (1) (January): 1–10. doi:10.1016/j.engfailanal.2007.12.001. <http://dx.doi.org/10.1016/j.engfailanal.2007.12.001>.
- Woolley, RL. 1953. "LXIV. The Bauschinger Effect in Some Face-Centred and Body-Centred Cubic Metals." *Philosophical Magazine*. <http://arch.neicon.ru/xmlui/handle/123456789/1620470>.

- Xiang, Y., and J.J. Vlassak. 2005. "Bauschinger Effect in Thin Metal Films." *Scripta Materialia* 53 (2) (July): 177–182. doi:10.1016/j.scriptamat.2005.03.048.
<http://linkinghub.elsevier.com/retrieve/pii/S1359646205002174>.
- Xue, Y, M Horstemeyer, D McDowell, H Elkadiri, and J Fan. 2007. "Microstructure-Based Multistage Fatigue Modeling of a Cast AE44 Magnesium Alloy." *International Journal of Fatigue* 29 (4) (April): 666–676. doi:10.1016/j.ijfatigue.2006.07.005.
<http://linkinghub.elsevier.com/retrieve/pii/S0142112306002040>.
- Xue, Y., C. L. Burton, M. F. Horstemeyer, D. L. McDowell, and J. T. Berry. 2007. "Multistage Fatigue Modeling of Cast A356-T6 and A380-F Aluminum Alloys." *Metallurgical and Materials Transactions B* 38 (4) (September 19): 601–606. doi:10.1007/s11663-007-9062-1. <http://link.springer.com/10.1007/s11663-007-9062-1>.
- Xue, Y., H. El Kadiri, M.F. Horstemeyer, J.B. Jordon, and H. Weiland. 2007. "Micromechanisms of Multistage Fatigue Crack Growth in a High-Strength Aluminum Alloy." *Acta Materialia* 55 (6) (April): 1975–1984. doi:10.1016/j.actamat.2006.11.009.
<http://linkinghub.elsevier.com/retrieve/pii/S1359645406008093>.
- Xue, Y., D.L. McDowell, M.F. Horstemeyer, M.H. Dale, and J.B. Jordon. 2007. "Microstructure-Based Multistage Fatigue Modeling of Aluminum Alloy 7075-T651." *Engineering Fracture Mechanics* 74 (17) (November): 2810–2823. doi:10.1016/j.engfracmech.2006.12.031.
<http://linkinghub.elsevier.com/retrieve/pii/S0013794407000227>.
- Xue, Y., a. Pascu, M.F. Horstemeyer, L. Wang, and P.T. Wang. 2010. "Microporosity Effects on Cyclic Plasticity and Fatigue of LENSTM-Processed Steel." *Acta Materialia* 58 (11) (June): 4029–4038. doi:10.1016/j.actamat.2010.03.014.
<http://linkinghub.elsevier.com/retrieve/pii/S135964541000159X>.
- Xue, Yibin, Amanda M. Wright, David L. McDowell, Mark F. Horstemeyer, Kiran Solanki, and Youssef Hammi. 2010. "Micromechanics Study of Fatigue Damage Incubation Following an Initial Overstrain." *Journal of Engineering Materials and Technology* 132 (2): 021010. doi:10.1115/1.4000227. <http://link.aip.org/link/JEMTA8/v132/i2/p021010/s1&Agg=doi>.
- Yoshida, Fusahito, and Takeshi Uemori. 2002. "A Model of Large-Strain Cyclic Plasticity Describing the Bauschinger Effect and Workhardening Stagnation." *International Journal of Plasticity* 18 (5-6) (October): 661–686. doi:10.1016/S0749-6419(01)00050-X.
<http://linkinghub.elsevier.com/retrieve/pii/S074964190100050X>.
- Yoshimura, Y, T Daigaku, and K Kenkyjo. 1959. *Hypothetical Theory of Anisotropy and the Bauschinger Effect due to Plastic Strain History*.
<http://repository.tksc.jaxa.jp/dr/prc/japan/contents/IS2404821000/IS2404821.pdf>.

Yoshimura, Y, and K Kenkyūjo. 1959. *Theory of Plasticity for Small and Finite Deformations Based on Legitimate Concept of Strain*. Vol. 348. Tokyo.
<http://repository.tksc.jaxa.jp/dr/prc/japan/contents/IS2404818000/IS2404818.pdf>.

Zhao, Qinglong. 2013. “The Influence of Mn, Fe and Si on the Work Hardening of Aluminum Alloys” (February). <http://ntnu.diva-portal.org/smash/get/diva2:599794/FULLTEXT03>.